Mixed radiated magneto Casson fluid flow with Arrhenius activation energy and Newtonian heating effects: Flow and sensitivity analysis

Zahra Abdelmalek [a,b], B. Mahanthesh [c], Md Faisal Md Basir [d], Maria Imtiaz [e], Joby Mackolil [c], Noor Saeed Khan [f], Hossam A. Nabwey [g,h], I. Tlili [i,*]

[a] *Institute of Research and Development, Duy Tan University, Da Nang 550000, Vietnam*
[b] *Faculty of Medicine, Duy Tan University, Da Nang 550000, Vietnam*
[c] *Department of Mathematics, CHRIST (Deemed to be University), Bangalore 560029, Karnataka, India*
[d] *Department of Mathematical Sciences, Faculty of Science, Universiti Teknologi Malaysia, 81310 UTM Johor Bahru, Malaysia*
[e] *Department of Social and Behavioral Sciences, National University of Medical Sciences, Rawalpindi, Pakistan*
[f] *Department of Mathematics, Abdul Wali Khan University, Mardan 23200, Khyber Pakhtunkhwa, Pakistan*
[g] *Department of Mathematics, College of Science and Humanities in Al-Kharj, Prince Sattam bin Abdulaziz University, Al-Kharj 11942, Saudi Arabia*
[h] *Department of Basic Engineering Science, Faculty of Engineering, Menoufia University, Shebin El-Kom 32511, Egypt*
[i] *Department of Mechanical and Industrial Engineering, College of Engineering, Majmaah University, Al-Majmaah 11952, Saudi Arabia*

Abstract The characteristics of Stefan blowing effects in a magneto-hydrodynamic flow of a Casson fluid past a stretching sheet are investigated. The effects of radiation, heat source/sink, Newtonian heating, Arrhenius activation energy and binary chemical reaction are considered for heat and mass transfer analysis. The homotopy analysis method (HAM) was utilised to solve the transformed non-dimensionalized equations analytically. The impact of various physical parameters affecting the flow are investigated. Further, the relationship of various parameters on the skin friction and rate of heat and mass transfer was explored using correlation and probable error. A sensitivity analysis was carried out based on the Response Surface Methodology to analyse the effect of Stefan blowing parameter, magnetic parameter and stretching/shrinking parameter on the reduced Nusselt number and reduced Sherwood number. A constant positive sensitivity for the reduced Nusselt number towards the Stefan blowing parameter for all levels of magnetic parameter and

---

* Corresponding author: Department of Mechanical and Industrial Engineering, College of Engineering, Majmaah University, Al-Majmaah 11952, Saudi Arabia.
E-mail address: l.tlili@mu.edu.sa (I. Tlili).

stretching/shrinking parameter was found. Further, the reduced Sherwood number indicated a negative sensitivity towards the Stefan blowing parameter.

1. Introduction

Non-Newtonian fluids are recognized as the major consuming fluids in daily lives. In the application of magnetohydrodynamics, the non-Newtonian fluids and plasma need sharp investigations since magnetic field appears on sun with high intensity in plasma where chemical reaction takes place every time. Sun surface is a major source of magnetic field and solar radiation prevailing plasma. Magnetic field establishes the powers to nanoparticles and any destiny. In the meantime, activation energy introduced by Arrhenius in 1889 confers the minimum powers of functioning the chemical reaction. Likewise, tasking the above, making a federally entity, Newtonian heating has the powers devolved which cannot be withdrawn in thermal system. In such a situation, entropy generation or thermal system disorderedness arises which cannot be ignored. Researchers are fully dedicated to measure the analysis accurately, even to measure the probable error and statistical declaration as well as sensitivity analysis to explore such complicated systems. Hayat et al. [1] pleaded that the apex study has declared that holding melting parameter amendments from time to time is necessary to ensure protection of higher velocity and less temperature. Hayat et al. [2] administrated that elected representatives appoint that the thermal relaxation parameter has struck down the temperature. Khan et al. [3] released a study that has satisfactory answers during the course of an investigation to the Hartman number. Hayat et al. [4] announced that speaking at the carbon nanotubes mobilizing has sought time to enable thermophysical properties so that the particles actively participate in the thermodynamics. Khan et al. [5] booked the disorderedness case and handed down the dragging behaviour for aluminium oxide. Hayat et al. [6] conveys the report to take along the entire effects like Joule heating and viscous dissipation in nanofluid flow and heat transfer in rotatory system. Rashid et al. [7] delegated to track down the magneto nanoliquid in which the thermal system disorderedness is credited for the Brinkman number with accomplishing the task. Hayat et al. [8] listed Cattaneo-Christov heat flux model due to the unavailability of some effects in common heat transfer equation. Qayyum et al. [9] negotiated under system disorderedness by Williamson fluid to deal with two rotating disks. Hayat et al. [10] reviewed the note that proposal of deferring quantities of parameters plan to calculate statistical declaration and probable error. The other related studies can be seen in [11–14].

Non-Newtonian fluids are employed in pharmaceutical products, polymer fluids, synovial liquids, animal blood, food processing etc. The Casson fluid model is a non-Newtonian model which was formulated by Casson [15] in 1959. He introduced this model for pigment oil suspensions of printing inks. It is a shear-thinning fluid where viscosity and the rate of shear are inversely proportional. Other fluids with similar properties such as jelly, ketchup and honey can be modelled quite well by the Casson fluid model. Interestingly, even blood flow in cap-

illary vessels can be characterised using the Casson fluid model due to the presence of red corpuscles, fibrinogens and proteins [16–18]. This has resulted in the Casson fluid model being used to improve the apparatus used for blood oxygenators and blood-dialysers. Shehzad et al. [19] considered the effects of internal heat generation and radiation for the flow of a Casson fluid past a stretched surface. They reported that the rise in the Casson fluid parameter led to an enhancement in thermal boundary layer thickness, whereas a decrement was observed for skin friction, Nusselt number and velocity. The radiative flow of a Casson fluid (non-aligned) was investigated by Mehmood et al. [20]. They employed the shooting method coupled with Runge-Kutta Fehlberg method to solve the governing equations. Other recent studies of Casson fluids can be found in [21–23].

Various technological processes such as permeability of microporous media, lubrication and the modelling of the blood flow through capillaries require an extensive understanding of the boundary slip. It is the non-adherence of fluids which give rise to the slip boundary conditions. The effects of thermal radiation on the heat transfer phenomenon have drawn the attention of researchers because of its importance in applications involving enormous temperatures such as propulsion devices for aircraft, nuclear reactors, solar power plants, metallurgical industries and so on. Due to the applications mentioned above, Seth, Mishra [24] analysed the time-dependent MHD flow of a nanofluid past a stretching surface with thermal radiation. They also utilised the Navier's slip boundary condition and reported that an increment in velocity slip would enhance the rate of heat transfer. The solutions were obtained using the Galerkin finite element technique. Slip effects along with magnetic field and thermal radiation were analysed by Besthapu et al. [25]. A drag reduction at the sheet was observed by using a porous medium along with the slip effects. The effect of radiation and Stefan blowing on the flow of a plane Poiseuille fluid with nanoparticles considering slip effects were studied by Alamri et al. [26]. Heat and mass transfer was also considered in the analysis. They reported that the second-order slip is more sensitive to the velocity field when compared to the first-order slip. Some studies on thermal radiation and slip effect can be seen in [27–29] and the references therein.

Swante Arrhenius pioneered the development of activation energy in 1889. The minimum energy required for atoms to initiate a chemical reaction is called activation energy. It finds applications in the mechanics of oil emulsions and geothermal engineering. Recently, Irfan et al. [30] analysed the effects of Arrhenius activation energy and chemical reaction on the three-dimensional flow of a Carreau nanofluid. The radiated Couette-Poiseuille flow in a horizontal channel with the magnetic field was investigated by Zeeshan et al. [31]. The approximate analytical Homotopy analysis method was utilised to solve the governing partial differential equations. They reported that chemical reaction and activation energy have

an opposite effect on the channel for Sherwood number. Recently, the impact of entropy generation in a Prandtl-Eyring nanofluid with heat source/sink and the activation energy was explored by Khan et al. [32]. Other recent investigations about the effect of Arrhenius activation energy on flows of various fluids can be found in [33–35].

The heat transfer at a surface in realistic cases is directly proportional to the local surface temperature. Newtonian heating is a crucial aspect of solar radiators, heat exchangers and heat transfer in fins. The two-dimensional flow of a third-grade nanofluid with Newtonian heating and viscous dissipation was investigated by Shehzad et al. [36]. They concluded that the increase in Newtonian heating parameter would lead to an increment in temperature. Later, Qayyum et al. [37] investigated the non-linear convective flow of a Powell-Erying nanofluid with Newtonian heating in the presence of a magnetic field. Recently, the effect of Newtonian heating on the flow of a water-based carbon nanotube nanofluid in a microchannel was analysed by Khan et al. [38]. The approximate-analytical solutions were obtained using Laplace transform with the Zakian's algorithm. Some studies on Newtonian heating and its impact on the flow of various types of fluids can be seen in [39–41].

The Homotopy Analysis Method (HAM) is an established approximate analytical method to tackle non-linear differential equations. This method uses the concept of homotopy to generate a convergent series of solutions. The auxiliary variables control the region of convergence. The 3-D flow of a Jeffrey nanofluid induced by a thermally radiative surface with Newtonian heating was analysed by Shehzad [42] using HAM. The hydromagnetic flow of a Carreau nanofluid and the variations in entropy generation was analysed by Khan et al. [43] employing the HAM.

Khan et al. [44] used BVP4C built-in function in MATLAB to solve the MHD radiative flow of Casson fluid toward a chemically reactive stretched surface, but their work did not take into consideration the Stefan blowing, Newtonian heating, slips and mass convective boundary conditions. A study about the effect of Stefan blowing on the MHD slip Casson fluid flow over a stretching surface with radiation, slips, Newtonian heating, convective mass, chemical reaction and Arrhenius activation energy with heat source/sink, so far as we are aware, has not been conducted yet. Casson fluid models are often used as rheological models for blood flows in arteries. Thus, it is conceivable that the mathematical model considered in this paper (which involves chemical reaction and radiation) may be used in an application involving blood-related diseases or drug delivery using blood. A study of the simultaneous effects of a chemical reaction and activation energy in relation to a model of blood flow was conducted by Ellahi et al. [45]. Their study was a study of remedies for malign tissues, cells or clogged arteries of the heart.

The aforementioned literature have taken up the talk of dissolution of Newtonian, non-Newtonian and nanofluids cases to decide the facts of around all representatives which were elected for the third tier of the problems insights. The authors have dissolved the problem to introduce a new local body setup. Several effects, including correlation and probable error, response surface methodology, activation energy challenging the flow, heat and mass transfer with thermal disorderedness and sensitivity analysis for the declaration of parameters have not been yet notified in the literature.

So the main objectives of the paper are to:

- utilize HAM to arrive at the solutions.
- scrutinize the impacts of different parameters on the velocity, temperature and concentration profiles of Casson fluids through graphs.
- utilize correlation and probable error to study the relationship of various parameters with the Nusselt number, Sherwood number and skin friction.
- run a response surface methodology (RSM) to analyse the sensitivity of the reduced Nusselt number and Sherwood number towards the chosen factor parameters.

2. Mathematical framework

2.1. Flow, heat and mass transfer analysis

As in Khan et al. [44], binary chemical reaction with Arrhenius activation energy in MHD mixed convection flow towards a stretched sheet is considered. The MHD stagnation point flow occurs for $y > 0$. The fluid is electrically conducting due to an applied magnetic field. The induced magnetic field is effectively zero on account of the small Reynolds number. The coordinate system is such that the $x-$axis is in stretching direction ($x-$axis) and the $y-$axis is perpendicular to it (normal). The flow geometry problem is shown in Fig. 1.

Suppose that at the surface of the sheet, the concentration of the fluid is denoted by C_f, while temperature and concentration at infinity are denoted as T_∞ and C_∞ respectively. The heat and mass transfer process are examined through thermal radiation and heat source/sink. Furthermore, Stefan is blowing, slips and Newtonian heating are is also considered. Along the $x-$axis, the velocity of the sheet is $\bar{u}_w = a\bar{x}$. The rheological equation for the considered fluid model is [47]

$$\tau_{ij} = \begin{cases} 2\left(\mu_B + \frac{P_y}{\sqrt{2\pi}}\right), & \pi > \pi_c \\ 2\left(\mu_B + \frac{P_y}{\sqrt{2\pi_c}}\right), & \pi < \pi_c \end{cases} \tag{1}$$

where

$\pi = e_{ij}, e_{ij}$:(i, j)-component of deformation rate,
π: product based on the non-Newtonian fluid,
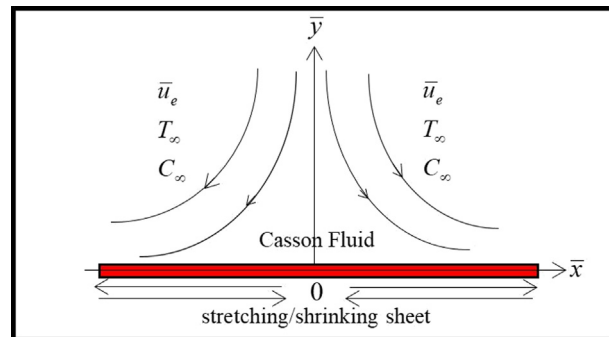π_c: critical value of this product,

Fig. 1 Geometry of the Problem (Adapted from Kumar et al. [46]).

μ_B: plastic dynamic viscosity of the non-Newtonian fluid,
P_y: yield stress of fluid

Modified from Kataria, Patel [48], yields

$$\frac{\partial \bar{u}}{\partial \bar{x}} + \frac{\partial \bar{v}}{\partial \bar{y}} = 0 \tag{2}$$

$$\bar{u}\frac{\partial \bar{u}}{\partial \bar{x}} + \bar{v}\frac{\partial \bar{u}}{\partial \bar{y}} = v\left(1 + \frac{1}{\beta}\right)\frac{\partial^2 \bar{u}}{\partial \bar{y}^2} + \bar{u}_e\frac{d\bar{u}_e}{d\bar{x}} + \frac{\sigma B_0^2(\bar{u}_e - \bar{u})}{\rho}$$
$$+ g(\beta_T(T - T_\infty) + \beta_C(C - C_\infty)) \tag{3}$$

$$\bar{u}\frac{\partial T}{\partial \bar{x}} + \bar{v}\frac{\partial T}{\partial \bar{y}} = \alpha\frac{\partial^2 T}{\partial \bar{y}^2} + \frac{Q_0(T - T_\infty)}{(\rho c_p)_f} + \frac{16\sigma_1 T_\infty^3}{3k^*(\rho c_p)_f}\frac{\partial^2 T}{\partial \bar{y}^2} \tag{4}$$

$$\bar{u}\frac{\partial C}{\partial \bar{x}} + \bar{v}\frac{\partial C}{\partial \bar{y}} = D\frac{\partial^2 C}{\partial \bar{y}^2} - k_r^2(C - C_\infty)\left(\frac{T}{T_\infty}\right)^m \exp\left(\frac{-E_a}{K^* T}\right) \tag{5}$$

The conditions at the boundary are:

$$\bar{u} = \bar{u}_w + \bar{u}_{\text{slip}}, \quad \bar{v} = -\frac{D}{(1-C_f)}\frac{\partial C}{\partial \bar{y}}, \quad k\frac{\partial T}{\partial \bar{y}} = -h_s T,$$
$$-k_2\frac{\partial C}{\partial \bar{y}} = h_2(C_f - C) \qquad at\ y = 0 \tag{6}$$

$$\bar{u} = \bar{u}_e = c\bar{x}, \quad T = T_\infty, C = C_\infty \quad as\ y \to \infty \tag{7}$$

where u and v are components velocity at x and y axes respectively,

v: kinematic viscosity,
β: Casson fluid parameter,
u_e: free stream velocity,
σ: electrical conductivity,
B_0: magnetic field strength,
ρ: density,
g: gravitational acceleration,
β_T: coefficient of thermal expansion,
T: temperature of the fluid,
T_∞: ambient temperature,
β_C: coefficient of concentration expansion,
C: concentration,
C_∞: ambient concentration,
α: thermal diffusivity,
μ: dynamic fluid viscosity,
D: mass diffusion coefficient,
k_r: reaction rate,
m: fitted rate constant,
E_a: activation energy,
K^*: Boltzmann constant,
$\bar{u}_{\text{slip}} = N_1\left(1 + \frac{1}{\beta}\right)\frac{\partial \bar{u}}{\partial \bar{y}} + N_2\left(1 + \frac{1}{\beta}\right)\frac{\partial^2 \bar{u}}{\partial \bar{y}^2}$: velocity slip parameter,
u_w: stretching velocity.

Consider the following the similarity variables [47]

$$\eta = \sqrt{\frac{c}{v}}\bar{y}, \quad \bar{u} = c\bar{x}f'(\eta), \quad \bar{v} = -\sqrt{cv}f(\eta), \quad \theta(\eta)$$
$$= \frac{T - T_\infty}{T_\infty}, \quad \phi(\eta) = \frac{C - C_\infty}{C_f - C_\infty}. \tag{8}$$

where

c: stretching rate constant,
f': dimensionless velocity,
η: dimensionless variable,
θ: dimensionless temperature,
ϕ: dimensionless concentration,
T_f: fluid temperature.

Making use of (8), governing Eqs. (3) to (5) are converted into the following system of ordinary differential equations

$$\left(1 + \frac{1}{\beta}\right)f''' + 1 + M(1 - f') - f'^2 + ff'' + \lambda_1\theta + \lambda_2\phi = 0 \tag{9}$$

$$\frac{(1+R)}{\text{Pr}}\theta'' + f\theta' + Q_c\theta = 0 \tag{10}$$

$$\frac{1}{Sc}\phi'' + f\phi' - K_E(1 + \theta)^m\phi\exp\left(\frac{-E}{1+\theta}\right) = 0 \tag{11}$$

The transformed conditions at the boundary are as follows

$$f'(0) = \lambda + A\left(1 + \frac{1}{\beta}\right)f'' + B\left(1 + \frac{1}{\beta}\right)f''', \quad f(0) = s_1\frac{1}{Sc}\phi', \quad \theta'(0) = -\gamma(1 + \theta(0)),$$
$$\phi'(0) = -Bi_m(1 - \phi(0)) = 0 \tag{12}$$

$$f'(\infty) = 1, \quad \theta(\infty) = 0, \quad \phi(\infty) = 0 \tag{13}$$

where $M = \frac{\sigma B_0^2}{\rho c}$ magnetic parameter, $\lambda = \frac{a}{c}$ stretching/shrinking parameter, $\lambda_1 = \frac{Gr}{Re_x^2}$ thermal buoyancy parameter, $\lambda_2 = \frac{Gr^*}{Re_x^2}$ concentration buoyancy parameter, $Re_x = \frac{\bar{u}_e\bar{x}}{v}$ local Reynold number. $Gr = \frac{g\beta_T(T_f - T_\infty)\bar{x}^3}{v^2}$ local Grashof number due to temperature, $Gr^* = \frac{g\beta_C(C_f - C_\infty)\bar{x}^3}{v^2}$ local Grashof number due to concentration, $\text{Pr} = \frac{v}{\alpha}$ Prandtl number, $\alpha = \frac{k}{(\rho c_p)_f}$ thermal diffusivity, $v = \frac{\mu}{\rho}$ the kinematic diffusivity, k thermal conductivity, $Bi_m = \frac{h_2}{k_2}\sqrt{\frac{v}{c}}$ mass Biot number, $\gamma = \frac{h_s}{k}\sqrt{\frac{v}{c}}$ conjugate parameter for Newtonian heating, $\left(A = N_1\sqrt{\frac{c}{v}}\right) > 0$ first order slip velocity, $\left(B = N_2\frac{c}{v}\right) < 0$ second order slip velocity, $R = \frac{16\sigma^* T_\infty^3}{3kk^*}$ radiative parameter, $Q_c = Q_0/[\rho c_p]_f c$ heat source/sink parameter, $Sc = \frac{v}{D}$ Schmidt number, $K_E = \frac{k_r^2}{c}$ chemical reaction parameter, $s_1 = \frac{C_f - C_\infty}{1 - C_f}$ Stefan blowing parameter and $E = \frac{E_a}{K^* T_\infty}$ non-dimensional activation energy.

Here the positive values of s_1 represents for mass transfer from the sheet to the free stream (i.e. evaporation) and negative value of s_1 represents for the mass transfer from the free stream to the sheet wall. In short, for $s_1 > 0$ presents mass blowing at the sheet wall and $s_1 < 0$, presents the mass suction. Also, we *fixed* Pr = 21, which refers to human blood.

3. Quantities of physical interest

The quantities of physical interest are:

$$C_f = \frac{1}{\rho\bar{u}_w^2}\left(\mu_B + \frac{P_y}{\sqrt{2\pi}}\right)\frac{\partial \bar{u}}{\partial \bar{y}}\bigg|_{y=0} \tag{14}$$

$$Nu_x = \frac{q_w\bar{x}}{k(T_f - T_\infty)} \tag{15}$$

$$Sh_x = \frac{J_w \bar{x}}{D_B(C_f - C_\infty)} \tag{16}$$

where $q_w = -\left(k + \frac{16\sigma_1 T_\infty^3}{3k^*(\rho c_p)_f}\right)\frac{\partial T}{\partial y}\Big|_{y=0}$ and $J_w = -D_B\frac{\partial C}{\partial y}\Big|_{y=0}$ are heat and mass flux respectively.

In the non-dimensional form (14)–(16) can be presented as follows

$$C_f Re_x^{1/2} = \left(1 + \frac{1}{\beta}\right)f''(0) \tag{17}$$

$$Nu_x Re_x^{-1/2} = -(1 + R)\theta'(0) \tag{18}$$

$$Sh_x Re_x^{-1/2} = -\phi'(0) \tag{19}$$

where $Re_x = \frac{\bar{u}_e \bar{x}}{v}$ is local Reynold number.

4. Analysis of entropy generation

For the Casson fluid flow, the volumetric entropy generation equation in dimensional form can be written [49]

$$S_G = \frac{k}{T_\infty^2}\left(\frac{\partial T}{\partial y}\right)^2\left(1 + \frac{16\sigma^* T_\infty^3}{3kk^*}\right) + \left(1 + \frac{1}{\beta}\right)\frac{\mu}{T_\infty}\left(\frac{\partial \bar{u}}{\partial y}\right)^2$$
$$+ \frac{RD}{C_\infty}\left(\frac{\partial C}{\partial y}\right)^2 + \frac{\sigma B_0^2 \bar{u}^2}{T_\infty} + \frac{RD}{T_\infty}\left(\frac{\partial T}{\partial x}\frac{\partial C}{\partial y} + \frac{\partial C}{\partial y}\frac{\partial T}{\partial y}\right) \tag{20}$$

Using (8), dimensional Eq. (20) gets converted into the following dimensionless form

$$N_g = (1 + R)\alpha_1 \theta'^2 + \left(1 + \frac{1}{\beta}\right)Br f''^2 + Br M f'^2$$
$$+ L\left(\frac{\alpha_2}{\alpha_1}\phi'^2 + \phi'\theta'\right) \tag{21}$$

In the above expression (21), $N_G = \frac{S_G T_\infty v}{ak\Delta T}$ represents entropy generation rate, $\alpha_1 = \frac{(T_f - T_\infty)}{T_\infty}$ dimensionless temperature ratio variable, $Br = \frac{\mu a^2 \bar{x}^2}{k\Delta T}$ Brinkman number, $L = \frac{RD(C_f - C_\infty)}{k}$ diffusive variable and $\alpha_2 = \frac{(C_f - C_\infty)}{C_\infty}$ dimensionless concentration ratio variable.

5. Homotopy analysis method

For the velocity, temperature and concentration profiles, the initial approximations and linear operators obtained via trial and error are taken to be:

$$f_0(\eta) = \eta + \frac{\lambda - 1}{1 + A\left(1 + \frac{1}{\beta}\right) - B\left(1 + \frac{1}{\beta}\right)}(1 - e^{-\eta})$$
$$- \frac{s_1}{Sc}\left(\frac{Bi_m}{1 + Bi_m}\right)e^{-\eta}, \tag{22}$$

$$\theta_0(\eta) = \frac{\gamma}{1 - \gamma}e^{-\eta}, \tag{23}$$

$$\varphi_0(\eta) = \frac{Bi_m}{1 + Bi_m}e^{-\eta}, \tag{24}$$

$$L_f = f''' - f', L_\theta = \theta'' - \theta, L_\varphi = \varphi'' - \varphi, \tag{25}$$

with

$$L_f(c_1 + c_2 e^\eta + c_3 e^{-\eta}) = 0, L_\theta(c_4 e^\eta + c_5 e^{-\eta})$$
$$= 0, L_\varphi(c_6 e^\eta + c_7 e^{-\eta}) = 0, \tag{26}$$

where $c_1 - c_7$ are constants.

Let the embedding parameter be $p \in [0, 1]$ and auxiliary parameters by $\hbar_f$, $\hbar_\theta$ and $\hbar_\varphi$ then the zeroth order deformation equations are developed as follows:

$$(1 - p)L_f\left[\widehat{f}(\eta, p) - f_0(\eta)\right] = p\hbar_f N_f\left[\widehat{f}(\eta, p), \widehat{\theta}(\eta, p), \widehat{\varphi}(\eta, p)\right], \tag{27}$$

$$(1 - p)L_\theta\left[\widehat{\theta}(\eta, p) - \theta_0(\eta)\right] = p\hbar_\theta N_\theta\left[\widehat{\theta}(\eta, p), \widehat{f}(\eta, p), \widehat{\varphi}(\eta, p)\right], \tag{28}$$

$$(1 - p)L_\varphi[\widehat{\varphi}(\eta, p) - \varphi_0(\eta)] = p\hbar_\varphi N_\varphi\left[\widehat{\varphi}(\eta, p), \widehat{f}(\eta, p), \widehat{\theta}(\eta, p)\right]. \tag{29}$$

We define the nonlinear operators as

$$N_f\left[\widehat{f}(\eta, p), \widehat{\theta}(\eta, p), \widehat{\varphi}(\eta, p)\right] = \left(1 + \frac{1}{\beta}\right)\frac{\partial^3 \widehat{f}(\eta, p)}{\partial \eta^3} + 1$$
$$+ M\left(1 - \frac{\partial \widehat{f}(\eta, p)}{\partial \eta}\right)$$
$$- \frac{\partial \widehat{f}(\eta, p)}{\partial \eta}\frac{\partial \widehat{f}(\eta, p)}{\partial \eta}$$
$$+ \widehat{f}(\eta, p)\frac{\partial^2 \widehat{f}(\eta, p)}{\partial \eta^2}$$
$$+ \lambda_1 \widehat{\theta}(\eta, p) + \lambda_2 \widehat{\varphi}(\eta, p), \tag{30}$$

$$N_\theta\left[\widehat{\theta}(\eta, p), \widehat{f}(\eta, p), \widehat{\varphi}(\eta, p)\right] = \frac{1 + R}{Pr}\frac{\partial^2 \widehat{\theta}(\eta, p)}{\partial \eta^2}$$
$$+ \widehat{f}(\eta, p)\frac{\partial \widehat{\theta}(\eta, p)}{\partial \eta}$$
$$+ Q_c \widehat{\theta}(\eta, p), \tag{31}$$

$$N_\varphi\left[\widehat{\varphi}(\eta, p), \widehat{f}(\eta, p), \widehat{\theta}(\eta, p)\right] = \frac{1}{Sc}\frac{\partial^2 \widehat{\varphi}(\eta, p)}{\partial \eta^2} + \widehat{f}(\eta, p)\frac{\partial \widehat{\varphi}(\eta, p)}{\partial \eta}$$
$$- K_E\left((1 - E)\widehat{\varphi}(\eta, p) + (m + E - mE)\widehat{\theta}(\eta, p)\widehat{\varphi}(\eta, p)\right), \tag{32}$$

with boundary conditions

$$\widehat{f}(0, p) = \lambda + A\left(1 + \frac{1}{\beta}\right)\widehat{f}'(0, p) + B\left(1 + \frac{1}{\beta}\right)\widehat{f}''(0, p), \widehat{f}(0, p)$$
$$= s_1 \frac{1}{Sc}\widehat{\varphi}'(0, p),$$

$$\widehat{\theta}'(0, p) = -\gamma\left(1 + \widehat{\theta}(0, p)\right), \widehat{\varphi}'^{(0,p)} = -Bi_m(1 - \widehat{\varphi}(0, p)) = 0$$

$$\widehat{f}(\infty, p) = 1, \widehat{\theta}(\infty, p) = 0, \widehat{\varphi}(\infty, p) = 0 \tag{33}$$

The $mth-$ order deformation problems are

$$L_f[f_m(\eta) - \chi_m f_{m-1}(\eta)] = \hbar_f R_{f,m}(\eta), \tag{34}$$

$$L_\theta[\theta_m(\eta) - \chi_m \theta_{m-1}(\eta)] = \hbar_\theta R_{\theta,m}(\eta), \tag{35}$$

$$L_\varphi[\varphi_m(\eta) - \chi_m \varphi_{m-1}(\eta)] = \hbar_\varphi R_{\varphi,m}(\eta), \tag{36}$$

$$\chi_m = \begin{cases} 0, & m \leq 1 \\ 1, & m > 1 \end{cases}, \tag{37}$$

$$R_{f,m}(\eta) = \left(1 + \frac{1}{\beta}\right)f'''_{m-1} + (1 + M)(1 - \chi_m) - Mf'_{m-1}$$
$$+ \sum_{k=0}^{m-1}\left[f_{m-1-k}f''_k - f'_{m-1-k}f'_k\right] + \lambda_1\theta_{m-1}$$
$$+ \lambda_2\varphi_{m-1}, \tag{38}$$

$$R_{\theta,m}(\eta) = \frac{1 + R}{Pr}\theta''_{m-1} + \sum_{k=0}^{m-1}f_{m-1-k}\theta'_k + Q_c\theta_{m-1}, \tag{39}$$

$$R_{\varphi,m}(\xi) = \frac{1}{Sc}\varphi''_{m-1} + \sum_{k=0}^{m-1}\varphi'_{m-1-k}f_k$$
$$- K_E\left((1 - E)\varphi_{m-1} + (m + E - mE)\sum_{k=0}^{m-1}\varphi_{m-1-k}\theta_k\right), \tag{40}$$

$$f'_m(0) - A\left(1 + \frac{1}{\beta}\right)f''_m(0) - B\left(1 + \frac{1}{\beta}\right)f'''_m(0) = f_m(0) - \frac{s_1}{Sc}\varphi'_m(0)$$
$$= 0,$$

$$\theta'_m(0) + \gamma\theta_m(0) = \varphi'_m(0) - Bi_m\varphi_m(0) = f'_m(\infty) = \theta_m(\infty)$$
$$= \varphi_m(\infty) = 0 \tag{41}$$

The general solutions $(f_m, \theta_m, \varphi_m)$ comprising the special solutions $(f_m^*, \theta_m^*, \varphi_m^*)$ are given by

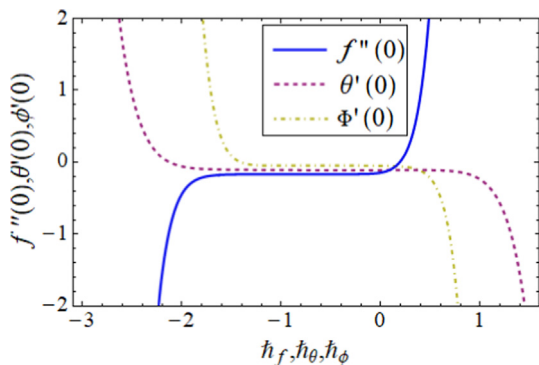$$f_m(\eta) = f_m^*(\eta) + c_1 + c_2e^\eta + c_3e^{-\eta},$$

Fig. 2 Combined $\hbar$ - curves for f'(0), θ'(0) and Φ'(0).

$$\theta_m(\eta) = \theta_m^*(\eta) + c_4e^\eta + c_5e^{-\eta},$$

$$\varphi_m(\eta) = \varphi_m^*(\eta) + c_6e^\eta + c_7e^{-\eta}. \tag{42}$$

6. Convergence analysis

The HAM convergence region is governed by auxiliary parameters $\hbar_f$, $\hbar_\theta$ and $\hbar_\varphi$. From Fig. 2 the $\hbar-$ curves are sketched to attain the valid domains i-e $[-1.6, -0.1]$, $[-1.9, -0.5]$ and $[-1, -0.2]$ are sufficient ranges of $\hbar_f$, $\hbar_\theta$ and $\hbar_\varphi$. Table 1 shows the convergence of series solutions of the problem considered.

7. Results and discussion

The effects of various involved parameters on fluid flow, temperature, volume fraction, skin friction coefficient, heat transfer rate, Sherwood number and entropy generation are scrutinised graphically.

7.1. Dimensionless velocity profile $f'(\eta)$

The effects of stretching parameter (λ), Casson fluid parameter (β), Hartman number (M) and Stefan blowing parameter (s_1) on fluid velocity $f'(\eta)$ are analysed in Figs. 3–6. Fig. 3 portrays the enhancement of velocity as λ is increased. The suppressing impact of β on the velocity is shown in Fig. 4. The increase in β causes a decrease in the boundary layer thickness which in turn causes a decrease in the velocity. The effect of M on $f'(\eta)$ is portrayed in Fig. 5. In non-dimensional form through Eq. (9), the magnetic field parameter is tied as - Mf' constituting a negative term which does a lot in affecting the motion. It is established that an increment in M leads to a decrease in velocity. This happens because of the retarding force by the induced Lorentz force. This decelerating force acts as a frictional resistance retarding the fluid flow. Fig. 6 shows a decrease in velocity as s_1 increases. Here, a positive value of s_1 represents injection and a negative value of s_1 represents suction at the wall. In the present case, the mass transfers as s_1 assumes the larger values. Due to greater quantities of mass, the velocity becomes slow.

7.2. Dimensionless temperature profile (θ)

The effects of Casson fluid parameter (β), conjugate parameter (γ), radiation (R) and heat source/sink parameter (Q_c) on temperature $\theta(\eta)$ are shown in Figs 7–10. Fig. 7 depicts the rise in

Table 1 Convergence of series solutions when. $s_1 = \beta = 0.9, B = -0.1, \lambda_1 = \lambda = M = Sc = m = 0.5, A = Q_c = K_E = Bi_m = \gamma = 0.1, E = 0.3, R = \lambda_2 = 0.7$ and $Pr = 21$.

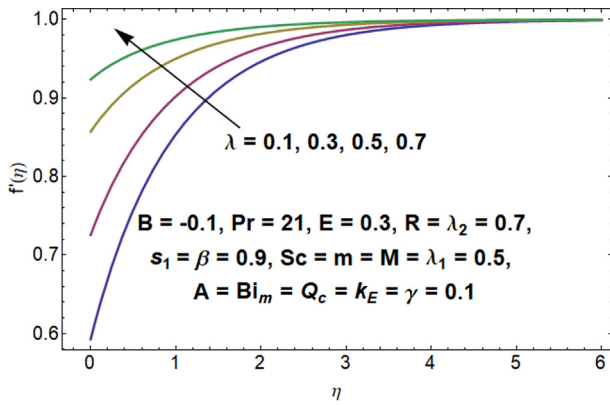| Order of approximations	−f'(0)	−θ'(0)	Φ'(0)
1	0.1989	0.1115	0.08819
5	0.2272	0.1140	0.08554
10	0.2341	0.1149	0.08437
15	0.2341	0.1166	0.08370
20	0.2341	0.1166	0.08319
25	0.2341	0.1166	0.08302
30	0.2341	0.1166	0.08302
40	0.2341	0.1166	0.08302

Fig. 3   Impact of the stretching parameter on velocity.
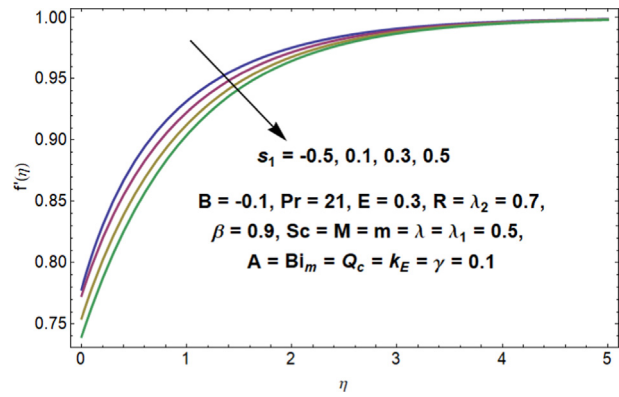

Fig. 6   Impact of the Stefan blowing parameter on velocity.
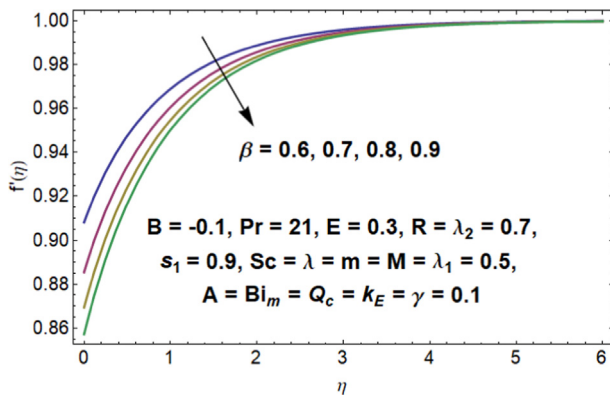

Fig. 4   Impact of the Casson fluid parameter on velocity.
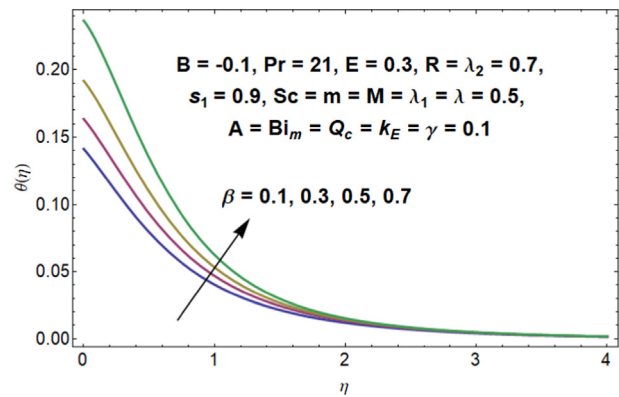

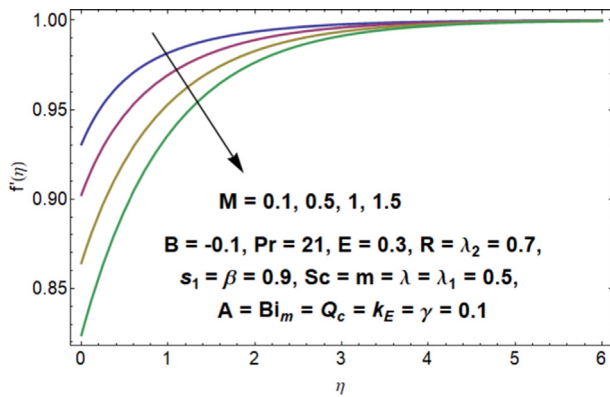**Fig. 7**   Impact of the Casson fluid parameter on temperature.

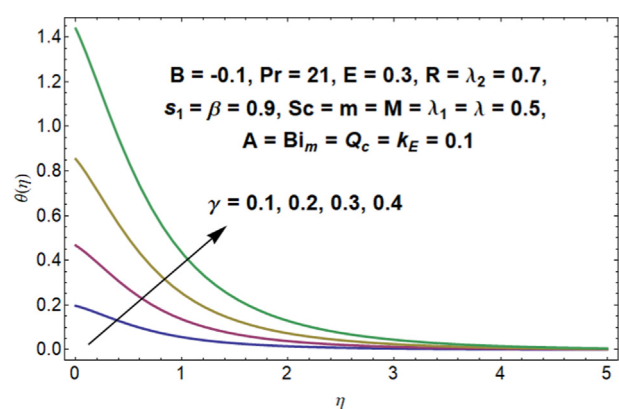**Fig. 5**   Impact of the magnetic field on velocity.

Fig. 8   Impact of the conjugate parameter on temperature.

temperature as the value of β is increased. Non-Newtonian behaviour favours the thermal systems in general. The impact of γ on $\theta(\eta)$ is presented in Fig. 8. The increase in γ leads to the enhancement of $\theta(\eta)$. This can be attributed to the dominance of viscous forces by the increase of the conjugate parameter. The enhancing effect of R on $\theta(\eta)$ is given in Fig. 9. As R is increased, the mean absorption coefficient reduces. This leads to an increment in the radiative heat transfer rate and therefore, $\theta(\eta)$ is enhanced. Moreover, these two quantities $(\theta(\eta), R)$ are interrelated to each other i. e. when one quantity is increased, the other one is automatically increased. Fig. 10

indicates the impact of the Q_c on $\theta(\eta)$. The heat source $(Q_c > 0)$ improves the thermal conductivity which leads to an enhancement in the fluid temperature. On the other hand, the heat sink $(Q_c < 0)$ leads to a decrease in the temperature of the fluid because of the decrement in thermal conductivity.

7.3. Dimensionless concentration profile $\phi(\eta)$

Figs. 11–15 depict the influence of fitted rate constant (m), activation energy (E), mass Biot parameter (Bi_m), chemical reac-
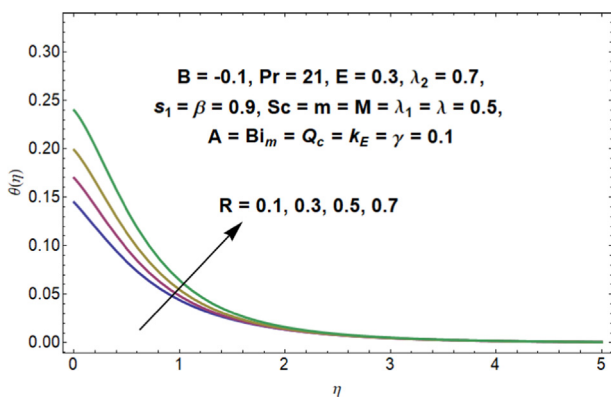
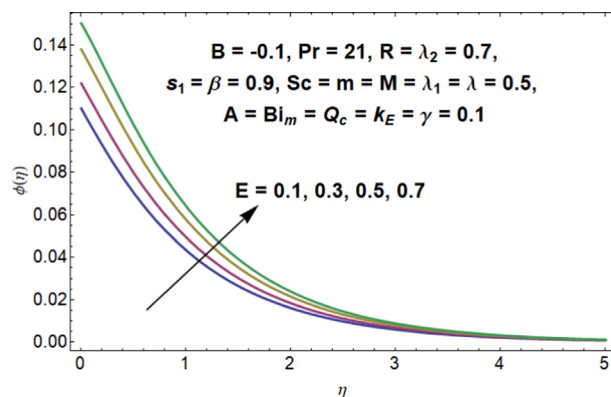**Fig. 9** Impact of the radiation parameter on temperature.

Fig. 12 Impact of the activation energy on concentration.
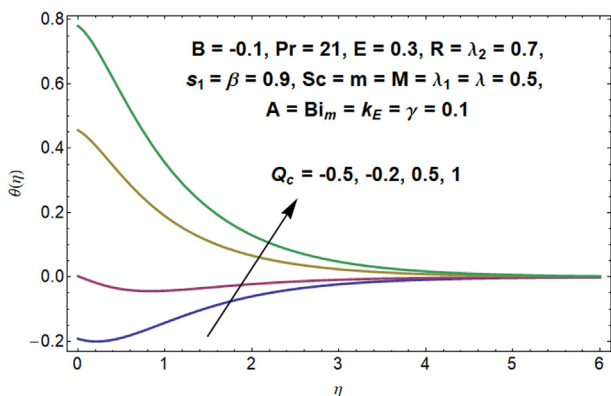

Fig. 10 Impact of the heat source/sink parameter on temperature.
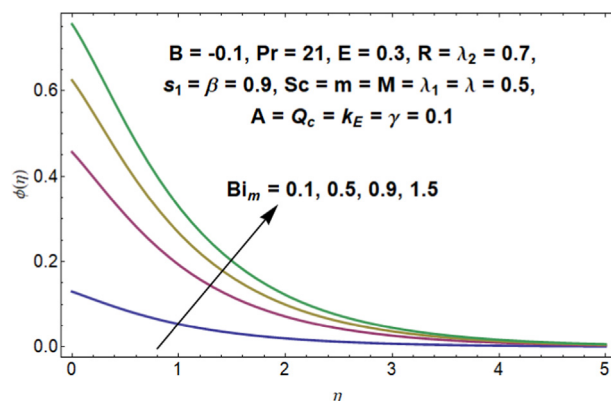

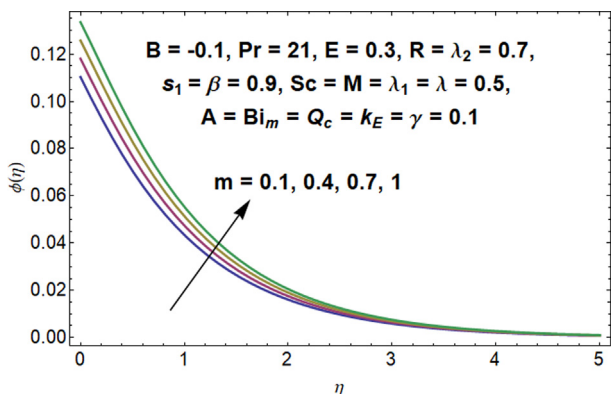**Fig. 13** Impact of the mass Biot parameter on concentration.

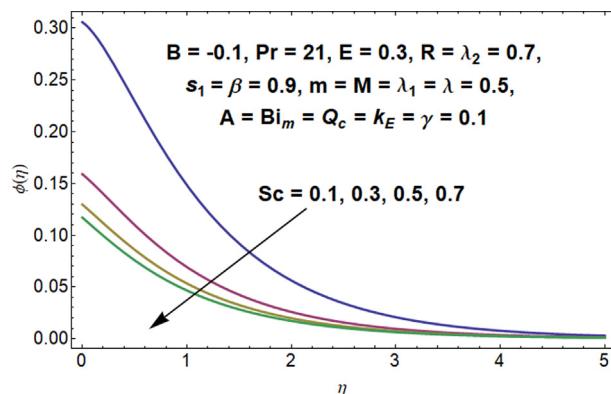**Fig. 11** Impact of the fitted rate constant on concentration.

Fig. 14 Impact of the Schmidt number on concentration.

tion parameter (k_E) and Schmidt number (Sc) on the concentration profile. Fig. 11 illustrates the marginal rise in concentration with respect to the increase in m. The impact of activation energy on the concentration profile is portrayed in Fig. 12. The enhancement of E leads to the decay of the modified Arrhenius function. Eventually, this endorses generative chemical reactions due to which concentration increases. The last term in Eq. (11) shows that $\phi \exp\left(\frac{-E}{1+\theta}\right)$ which is a better tool to check how the Arrhenius activation affects the

nanoparticle concentration. The influence of Bi_m on the concentration is depicted in Fig. 13. The increment in Bi_m intensifies the concentration. The thermal penetration depth increases as Bi_m is increased. Hence, the concentration profile is enhanced. The decreasing impact of Sc on concentration can be seen in Fig. 14. Physically, the increase of Sc causes a reduction in molecular diffusivity which leads to the increase of the concentration. The behaviour of concentration when k_E is enhanced is shown in Fig. 15. As expected, the chemical reaction parameter $k_E > 0$ leads to a reduction in concentration.
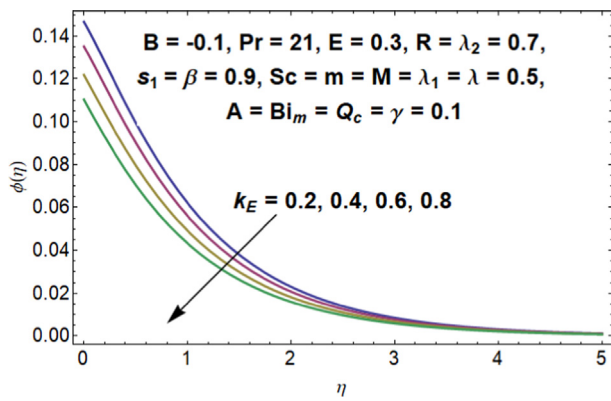
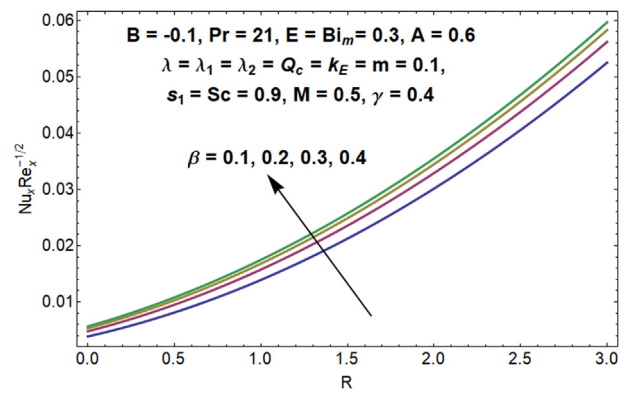**Fig. 15** Impact of the chemical reaction parameter on concentration.

Fig. 16 Impact of stretching and mass Biot parameters on the skin friction coefficient.

Fig. 17 Impact of Hartman number and Casson fluid parameter on the skin friction coefficient.

Fig. 18 Impact of radiation and Casson fluid parameters on the Nusselt number.

Fig. 19 Impact of chemical reaction and conjugate parameters on the Nusselt number.
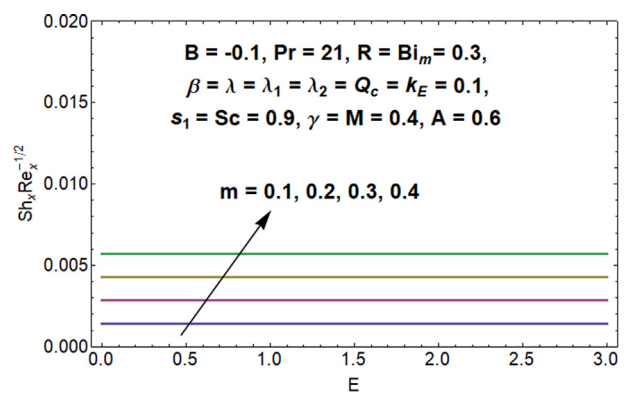
Fig. 20 Impact of fitted rate constant and activation energy on the Sherwood number.

7.4. Quantities of physical interest

The impacts of mass Biot number and stretching parameter on the skin friction coefficient $C_f Re_x^{1/2}$ are superimposed in Fig. 16. An enhancement in surface drag is observed when both λ and Bi_m are increased. Fig. 17 displays the change in $C_f Re_x^{1/2}$ for different values of Casson fluid parameter and

Hartman number. Surface drag force rises for higher Hartman number whereas it reduces for higher Casson fluid parameter.

The impacts of the radiation parameter and Casson fluid parameter on the Nusselt number $Nu_x Re_x^{-1/2}$ are shown in Fig. 18. It is observed that the heat transfer rate increases as both β and R are increased. Fig. 19 depicts the variation of $Nu_x Re_x^{-1/2}$ with respect to the changes in chemical reaction
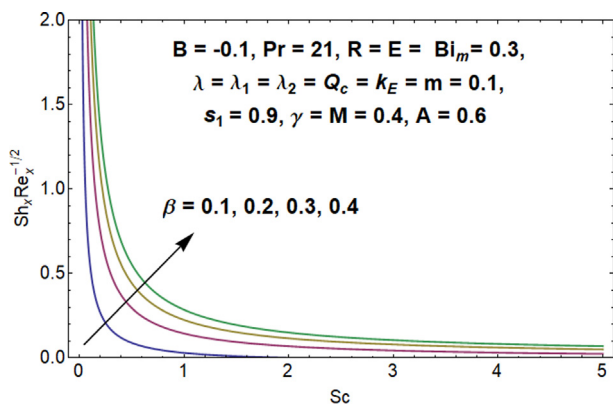
Fig. 21 Impact of Casson fluid parameter and Schmidt number on the Sherwood number.
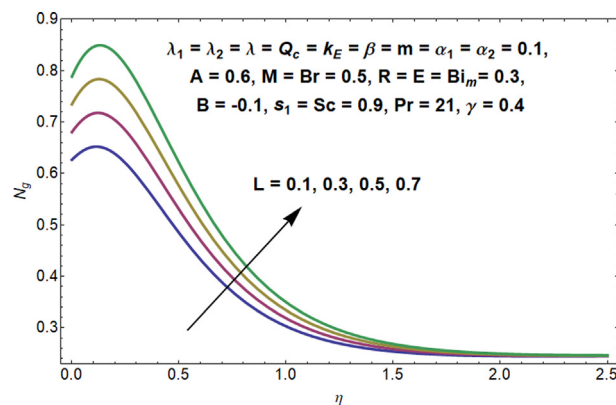
Fig. 24 Impact of the diffusive variable on the entropy generation rate.
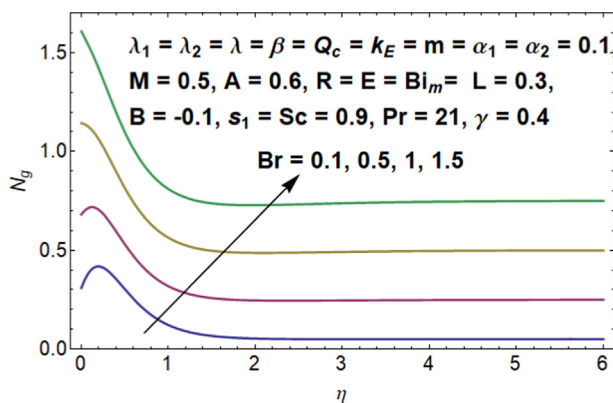
Fig. 22 Impact of the Brinkman number on the entropy generation rate.
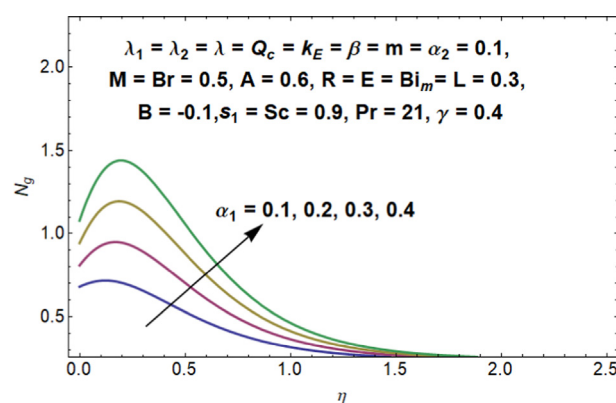
Fig. 25 Impact of the temperature ratio variable on the entropy generation rate.
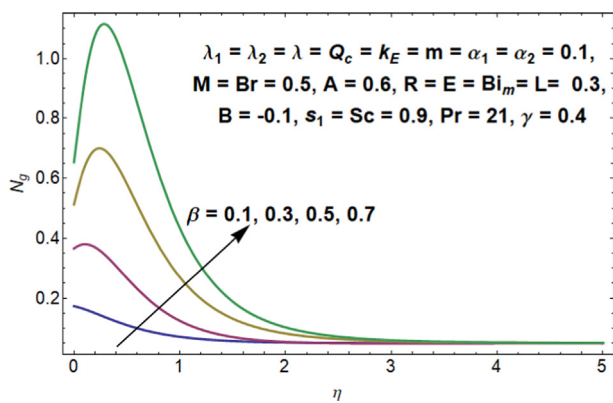
Fig. 23 Impact of the Casson fluid parameter on the entropy generation rate.
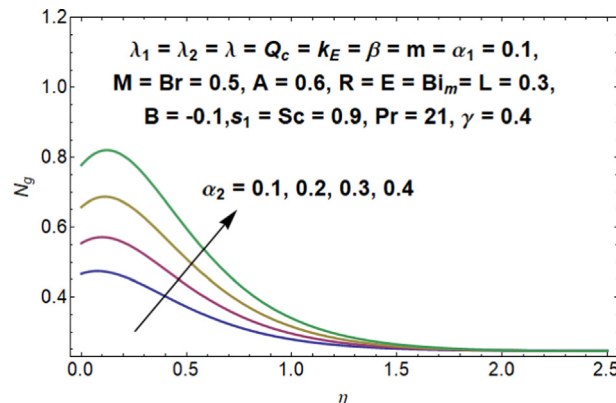
Fig. 26 Impact of the concentration ratio variable on the entropy generation rate.

and conjugate parameters on $Nu_x Re_x^{-1/2}$. The heat transfer rate accelerates for larger values of the conjugate parameter. The impact of chemical reaction parameter on $Nu_x Re_x^{-1/2}$ is very minimal.

The impacts of activation energy for various values of fitted rate constant on the mass transfer rate $Sh_x Re_x^{-1/2}$ are displayed in Fig. 20. There is an enhancement in Sherwood number when

m is increased. The combined effects of Sc and β on the local Sherwood number is displayed in Fig. 21. It is found that Sherwood the number is positively correlated to β while a negative correlation is observed for Sc.

The impacts of Brinkman number, Casson fluid parameter, diffusive variable, temperature ratio variable, concentration ratio variable and activation energy on the entropy generation

Fig. 27 Impact of the activation energy on the entropy generation rate.

rate (N_g) are shown in Figs. 22–27. It is noted that N_g improves for higher values of Br, β, L, α_1, α_2 and E.

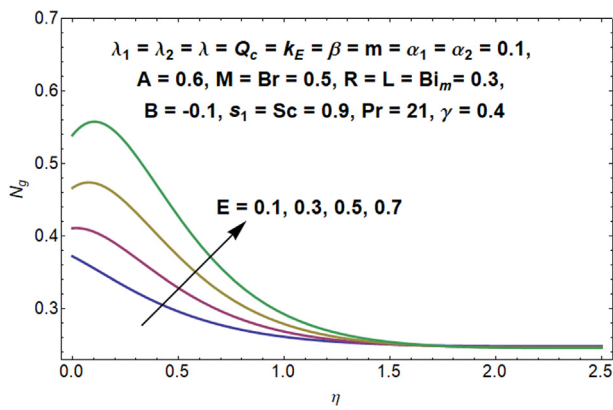### 7.5. Statistical analysis

Correlation is a statistical tool that measures the degree of relationship of variables. The correlation coefficient (r) quantifies the level of association of the variables considered. The probable error helps to verify whether the calculated correlation coefficient is significant. The probable error is calculated using the following formula:

$$PE = 0.6745\left(\frac{1-r^2}{\sqrt{n}}\right)$$

where n represents the number of observations [50]. When $\frac{r}{PE} > 6$, the correlation coefficient is said to be significant. The correlation coefficients of the parameters that affect the rate of heat transfer, Sherwood number and skin friction are presented in Table 2. From Table 2, it is concluded that $B, \beta, Q_c, K_E, m, s_1$ and Sc are positively correlated with Nu, whereas, $\lambda_1, \lambda_2, \lambda, M, A, Bi_m$ and γ are negatively correlated. These correlation coefficients are significant as $\frac{r}{PE} > 6$. It is also noted that the correlation coefficient calculated for E and Nu which is 0.0220 is not significant. Similarly, $\lambda_1, \lambda_2, Q_c, K_E, \lambda, m, M, A, R, Bi_m, Sc$ and γ are positively correlated to Sh and B, β, E and s_1 are negatively correlated to Sh. The parameters that are positively correlated to Cf are $B, \lambda_2, Q_c, M, R, E, Bi_m, s_1$ and γ. The parameters that are negatively correlated to Cf are $\lambda_1, \beta, K_E, m, A$ and Sc.

7.6. Response surface methodology

Response surface methodology (RSM) is a tool for sensitivity analysis. RSM throws light on the relationship between factor variables and one or more response variables. This method was devised by Box, Wilson [51]. Here, a face-centred Central Composite Design is utilised to study the relationship of Stefan blowing parameter (s_1), magnetic parameter (M) and stretching/shrinking parameter (λ (lambda)) with the response variables - Nu_x and Sh_x. The three factor variables and their levels are given in Table 3. The full quadratic model involving three linear terms, three interaction terms, three squared terms and an intercept term are given by:

Table 2 Correlation coefficient (r) of various parameters that affect (a) Nu (b) Sh and (c) Cf with their respective probable error (PE) and the ratio $\left|\frac{r}{PE}\right|$.

Parameter	r	PE	$\left|\frac{r}{PE}\right|$
(a) Nu			
B	0.9989	0.000665	1502.5
λ_1	−0.9735	0.015795	61.6
λ_2	−0.9993	0.000412	2423.2
B	0.9998	0.000093	10798.9
Q_c	0.9926	0.005764	172.2
K_E	0.9980	0.001175	849.1
λ	−0.9995	0.000318	3140.3
m	0.9993	0.000404	2474.1
M	−0.9982	0.001097	909.9
A	−0.8986	0.058072	15.5
E	0.0220	0.002698	0.1
Bi_m	−0.9955	0.055241	369.0
s_1	0.9038	0.019290	16.4
Sc	0.9675	0.089791	50.2
γ	−0.8381	0.055651	9.3
(b) Sh			
B	−0.9993	0.000403	2477.2
λ_1	0.9839	0.009626	102.2
λ_2	0.9999	0.000075	13276.4
β	−0.9915	0.005114	193.9
Q_c	0.9934	0.005124	193.9
K_E	0.9948	0.003108	320.1
λ	0.9999	0.000016	64498.5
m	0.9994	0.000371	2693.8
M	0.9981	0.001128	884.6
A	0.9201	0.046273	19.9
R	0.9937	0.003817	260.3
E	−0.9959	0.002483	401.1
Bi_m	0.9815	0.011035	88.9
s_1	−0.9999	0.000006	170619.2
Sc	0.9958	0.002547	391.0
γ	0.9516	0.028479	33.4
(c) Cf			
B	0.999172	0.000500	2000.2
λ_1	−0.01352	0.301590	0.0
λ_2	0.9999	0.000045	22003.7
β	−0.981690	0.010945	89.7
Q_c	0.974951	0.016684	58.4
K_E	−0.989	0.006602	149.8
m	−0.999	0.000605	1650.2
M	0.997045	0.001780	560.1
A	−0.92539	0.043331	21.4
R	0.999147	0.000514	1942.3
E	0.995586	0.002657	374.7
Bi_m	0.918581	0.047120	19.5
s_1	0.856647	0.080285	10.7
Sc	−0.84221	0.098034	8.6
γ	0.921513	0.045492	20.3

Table 3 Parameters with their levels.

Parameters	Symbol	Level		
		−1	0	1
s_1	A	0.1	0.6	1.1
M	B	0.5	1.5	2.5
λ	C	0.1	0.5	0.9

Table 4 Experimental Design and responses.

Runs	Coded Values			Real values			Response	
	A	B	C	s_1	M	λ	Nu_x	Sh_x
1	−1	−1	−1	0.1	0.5	0.1	0.471459	0.215981
2	1	−1	−1	1.1	0.5	0.1	0.783528	0.205723
3	−1	1	−1	0.1	2.5	0.1	0.216273	0.216854
4	1	1	−1	1.1	2.5	0.1	0.264827	0.206563
5	−1	−1	1	0.1	0.5	0.9	0.215817	0.217488
6	1	−1	1	1.1	0.5	0.9	0.259523	0.20734
7	−1	1	1	0.1	2.5	0.9	0.215819	0.217479
8	1	1	1	1.1	2.5	0.9	0.259692	0.207298
9	−1	0	0	0.1	1.5	0.5	0.216077	0.21711
10	1	0	0	1.1	1.5	0.5	0.262513	0.206872
11	0	−1	0	0.6	0.5	0.5	0.228379	0.211873
12	0	1	0	0.6	2.5	0.5	0.228133	0.212034
13	0	0	−1	0.6	1.5	0.1	0.229009	0.211546
14	0	0	1	0.6	1.5	0.9	0.227508	0.212385
15	0	0	0	0.6	1.5	0.5	0.228232	0.21197
16	0	0	0	0.6	1.5	0.5	0.228232	0.21197
17	0	0	0	0.6	1.5	0.5	0.228232	0.21197
18	0	0	0	0.6	1.5	0.5	0.228232	0.21197
19	0	0	0	0.6	1.5	0.5	0.228232	0.21197
20	0	0	0	0.6	1.5	0.5	0.228232	0.21197

Table 5 Analysis of variance for (a)Nu_x and (b)Sh_x.

Source	Degrees of freedom	Adjusted Sum of Squares	Adjusted Mean Square	F-Value	p-Value	
(a) Nu_x						
Model	9	0.288998	0.032111	7.2	0.002	Significant
Linear	3	0.146264	0.048755	10.93	0.002	Significant
s1	1	0.024467	0.024467	5.49	0.041	Significant
M	1	0.059902	0.059902	13.43	0.004	Significant
lambda	1	0.061896	0.061896	13.88	0.004	Significant
Square	3	0.04985	0.016617	3.73	0.049	Significant
s1*s1	1	0.00586	0.00586	1.31	0.278	Not Significant
M*M	1	0.003392	0.003392	0.76	0.404	Not Significant
lambda*lambda	1	0.003393	0.003393	0.76	0.403	Not Significant
Interaction	3	0.092884	0.030961	6.94	0.008	Significant
s1*M	1	0.008669	0.008669	1.94	0.193	Not Significant
s1*lambda	1	0.009319	0.009319	2.09	0.179	Not Significant
M*lambda	1	0.074896	0.074896	16.8	0.002	Significant
Error	10	0.044586	0.004459			
Lack-of-Fit	5	0.044586	0.008917	*	*	
Pure Error	5	0	0			
Total	19	0.333585				
$R^2 = 86.63\%$		Adjusted $R^2 = 74.6\%$				
(b) Sh_x						
Model	9	0.000265	0.000029	4518.52	0	Significant
Linear	3	0.000264	0.000088	13531.51	0	Significant
s1	1	0.000261	0.000261	40108.58	0	Significant
M	1	0	0	51.01	0	Significant
lambda	1	0.000003	0.000003	434.95	0	Significant
Square	3	0	0	3.81	0.047	Significant
s1*s1	1	0	0	0.29	0.605	Not Significant
M*M	1	0	0	1.7	0.221	Not Significant
lambda*lambda	1	0	0	1.12	0.315	Not Significant
Interaction	3	0	0	20.24	0	Significant
s1*M	1	0	0	0.08	0.778	Not Significant
s1*lambda	1	0	0	0.93	0.358	Not Significant
M*lambda	1	0	0	59.71	0	Significant
Error	10	0	0			
Lack-of-Fit	5	0	0	*	*	

Table 5 (*continued*)

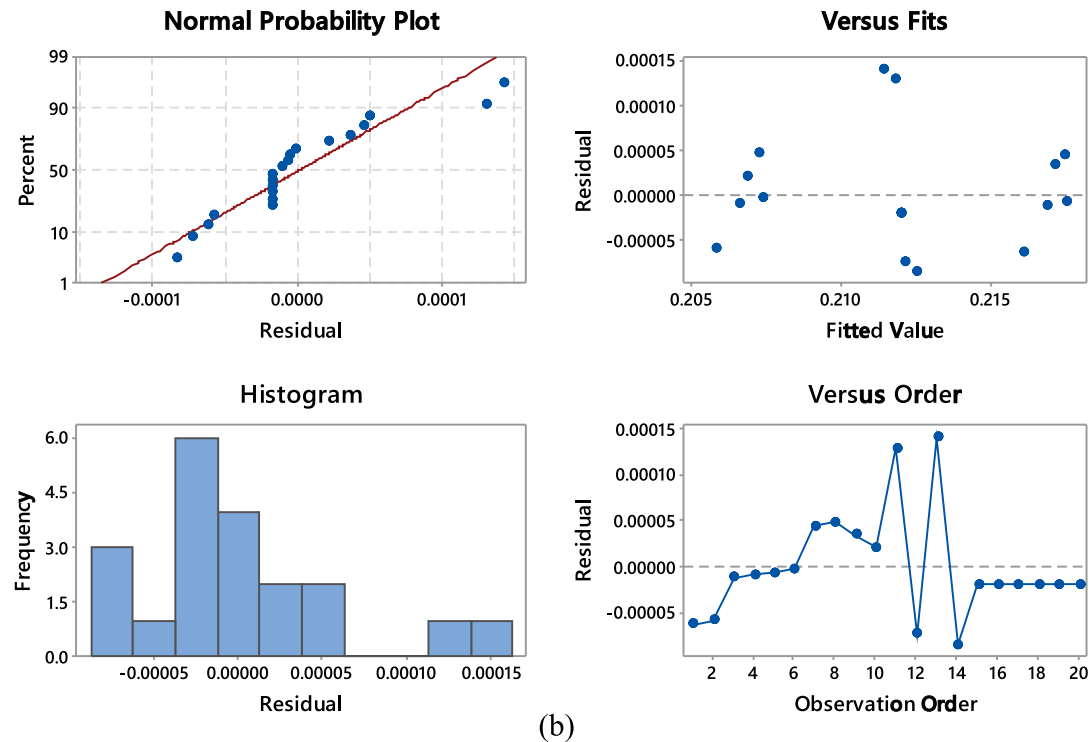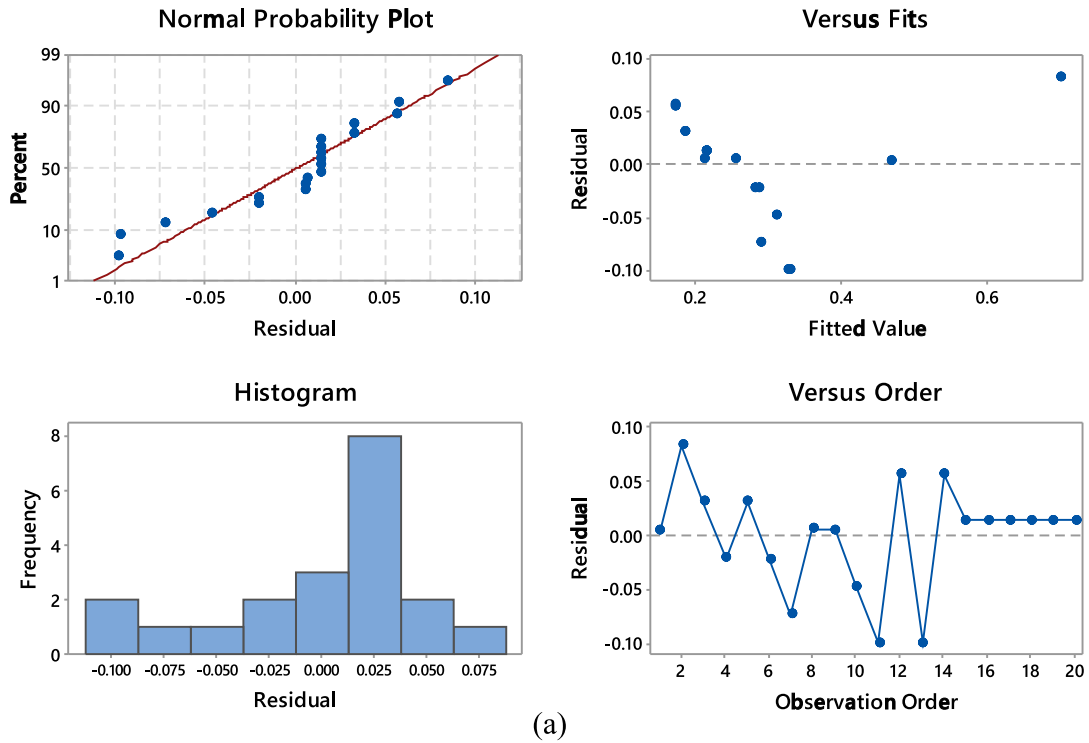| Source	Degrees of freedom	Adjusted Sum of Squares	Adjusted Mean Square	F-Value	p-Value
Pure Error	5	0	0		
Total	19	0.000265			
$R^2 = 99.98\%$		Adjusted $R^2 = 99.95\%$			

(a)

(b)

Fig. 28 Residual Plots for (a) Nu_x and (b) Sh_x.

Table 6 Regression coefficients of the RSM model for (a)Nu_x and (b)Sh_x.

Term	Coefficient	p-Value	
(a)Nu_x			
Constant	0.2142	0	Significant
s1	0.0495	0.041	Significant
M	−0.0774	0.004	Significant
lambda	−0.0787	0.004	Significant
s1*s1	0.0462	0.278	Not Significant
M*M	0.0351	0.404	Not Significant
lambda*lambda	0.0351	0.403	Not Significant
s1*M	−0.0329	0.193	Not Significant
s1*lambda	−0.0341	0.179	Not Significant
M*lambda	0.0968	0.002	Significant
(b)Sh_x			
Constant	0.211989	0	Significant
s1	−0.005112	0	Significant
M	0.000182	0	Significant
lambda	0.000532	0	Significant
s1*s1	−0.000026	0.605	Not Significant
M*M	−0.000063	0.221	Not Significant
lambda*lambda	−0.000051	0.315	Not Significant
s1*M	−0.000008	0.778	Not Significant
s1*lambda	0.000028	0.358	Not Significant
M*lambda	−0.00022	0	Significant

$$Response = a_{11}A^2 + a_{22}B^2 + a_{33}C^2 + a_{12}AB + a_{23}BC + a_{13}AC$$
$$+ a_1A + a_2B + a_3C + a_0.$$

where a_i and a_{ij} represent the regression coefficients. The twenty runs of the experimental design are in Table 4.

7.7. Accuracy of the model

The ANOVA table given in Table 5 is a measure of the accuracy for the estimated model. A parameter is significant (with 95% confidence) if the p-value is less than 0.05. In both the models, all the quadratic terms and the interaction terms involving s_1 are excluded as their p-value > 0.05 and hence are insignificant. However, the model for Sh_x proves to be a better one as its coefficient of determination (R^2) is higher (see Table 5). The high values of R^2 depict the accuracy of the models. Again, the residual plots in Fig. 28 are investigated. The Normal probability plots of Nu_x and Sh_x are aligned along the straight line and hence, the data is normal. 0.1 and 0.00015 are respectively the maximum deviations in the residuals versus fitted values plots for Nu_x and Sh_x, which adds to the accuracy of the model [52–54].

The regression coefficients for both the models are tabulated in Table 6. Considering the p-values, the significant variables are included in the models as given below:

$$Nu_x = 0.2142 + 0.0495s_1 - 0.0774M - 0.0787\lambda + 0.0968M*\lambda$$

$$Sh_x = 0.211989 - 0.005112s_1 + 0.000182M + 0.000532\lambda$$
$$- 0.00022M*\lambda$$

The response variables Nu_x and Sh_x are visualised as functions of s_1, M and λ in Figs. 29 and 30 using contour plots and 3-D surface plots. Fig. 29(a) shows the effect of s_1 and M on Nu_x. The highest rate of heat transfer is observed for the lower level of M and higher-level of s_1. The impact of s_1 and λ is presented in Fig. 29(b). The high level of s_1 and low level of λ maximises Nu_x. The low levels of both M and λ result in the highest rate of heat transfer (see Fig. 29(c)). As the values of M and λ increases, Nu_x reaches its minimum and then starts to increase.

Similarly, the impacts of s_1 and M on Sh_x are analysed in Fig. 30(a). Sh_x attains its highest value for the lower level of s_1 using all levels for M. It may also be noted that M has only a small impact on Sh_x as the change in Sh_x is nearly negligible as the level of M is incremented. The interaction of s_1 and λ is presented in Fig. 30(b) and it is observed that λ has only a nominal impact on the rate of mass transfer. On the other hand, Sh_x reaches its highest level at the lowest level of s_1. The effects of λ and M are also studied (see Fig. 30(c)). Comparatively, it is observed that λ has more impact on Sh_x than M. The highest rate of mass transfer is observed for the higher level of λ irrespective of the level of M. At, the lower level of λ an increasing trend for Sh_x is observed for an increment in M.

7.8. Sensitivity analysis

The partial derivative of the response functions with respect to the factors gives a measure of sensitivity. The sensitivity functions for Nu_x are:

$$\frac{\partial Nu_x}{\partial A} = 0.0495,$$

$$\frac{\partial Nu_x}{\partial B} = -0.0774 + 0.0968C,$$

$$\frac{\partial Nu_x}{\partial C} = -0.0787 + 0.0968B,$$

The sensitivity functions for Sh_x are:

$$\frac{\partial Sh_x}{\partial A} = -0.005112,$$

$$\frac{\partial Sh_x}{\partial B} = 0.000182 - 0.00022C,$$

$$\frac{\partial Sh_x}{\partial C} = 0.000532 - 0.00022B,$$

It may be noted that the sensitivity functions do not depend on A. The sensitivity of Nu_x and Sh_x for different levels of B and C when A is at the medium level ($A = 0$) are tabulated in Table 7. A positive value for the sensitivity represents an increase in the response variable when the factor variable is incremented and vice-versa. The sensitivity is visualised using bar charts. The sensitivity of Nu_x is given in Fig. 31. Clearly, Nu_x has a constant positive sensitivity for Stefan blowing parameter (coded as A). In Fig. 31(a), when the magnetic parameter is at the low level ($M = 0.5$), the sensitivity of Nu_x towards M is negative for the low level and medium level of stretching/shrinking parameter ($\lambda = 0.1$ and 0.5). But the sensitivity becomes positive when λ is at the high level ($\lambda = 0.9$). A reduction in the negative sensitivity of Nu_x towards M is observed when the level of λ changes from 0.1 to 0.5. At all levels of λ, the highest negative sensitivity of Nu_x is towards λ and the highest positive sensitivity is towards s_1. In Fig. 31
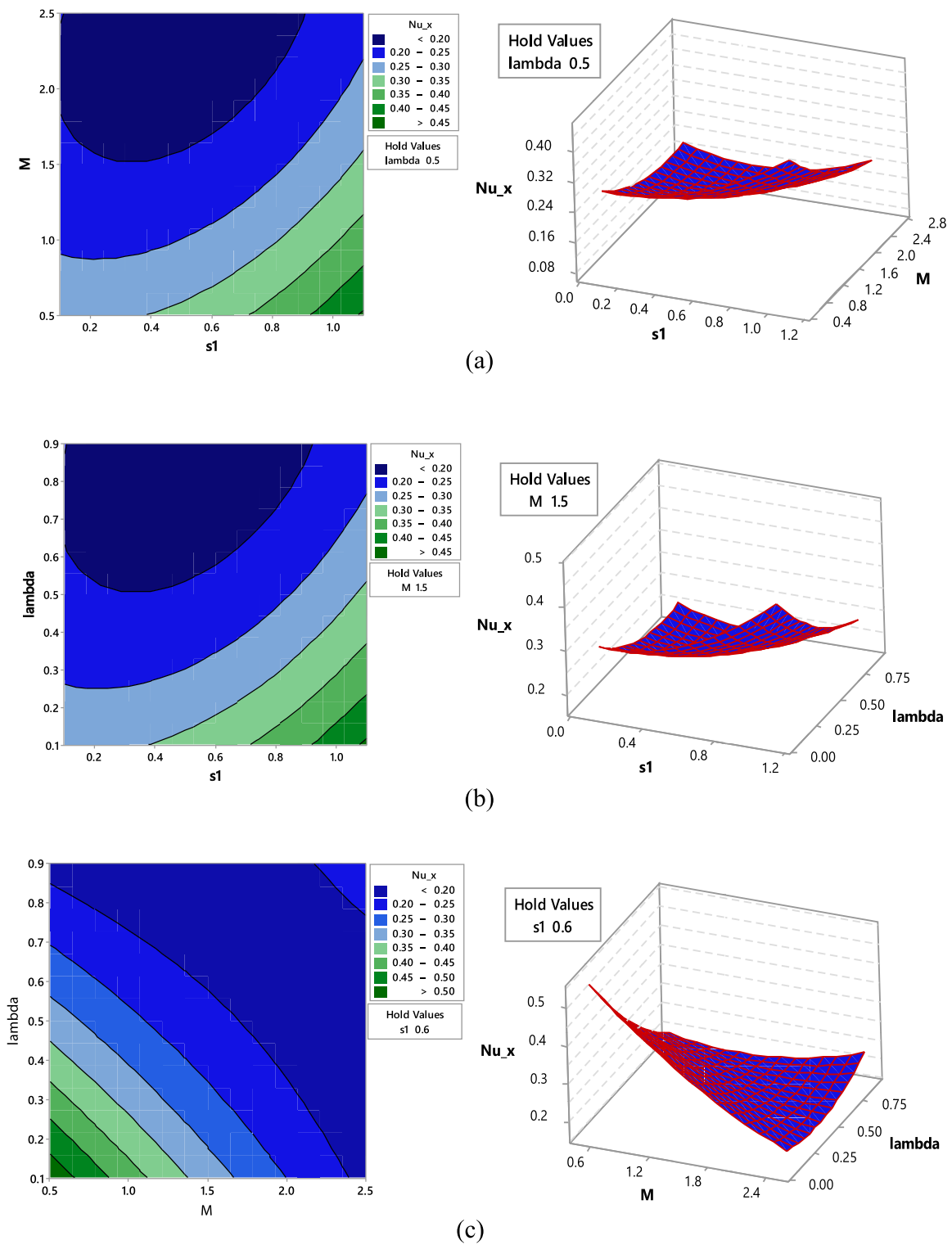
(a)

(b)

(c)

Fig. 29   Contour and surface plots for Nu_x.

(b) when the magnetic parameter is at the medium level ($M = 1.5$), the sensitivity of s_1 and M is found to be the same. But the constant negative sensitivity of Nu_x towards λ has reduced. Hence, when λ is at a low level ($\lambda = 0.1$), the highest negative sensitivity of Nu_x is for M. When M is at the high level (see Fig. 31(c)), a constant positive sensitivity of Nu_x towards λ is observed for all levels of λ.

The sensitivity of Sh_x is given in Fig. 32. Nu_x has a constant negative sensitivity for Stefan blowing parameter (coded as A) for all levels of M and λ. In Fig. 32(a), the sensitivity is visualised when M is at a low level ($M = 0.5$). The sensitivity of Sh_x to λ is positive and remains constant for different levels of λ. The sensitivity of Sh_x to M is positive but this decreases as the level of λ is increased from $\lambda = 0.1$ to $\lambda = 0.5$. When

(a)

(b)

(c)

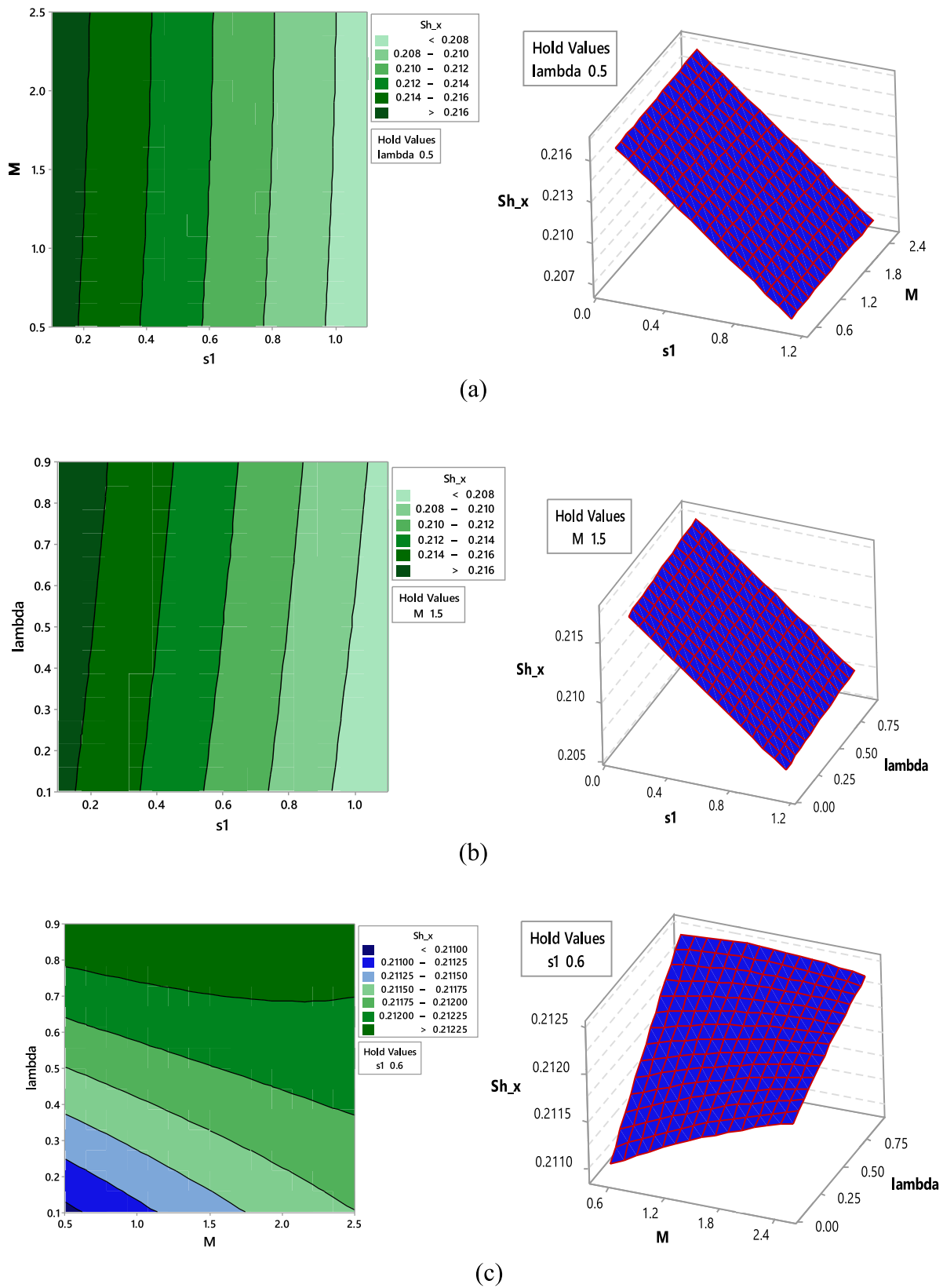**Fig. 30** Contour and surface plots for Sh_x.

$\lambda = 0.9$, the sensitivity of Sh_x towards M becomes negligible. For all levels of λ, the highest negative sensitivity of Sh_x is towards s_1 and the highest positive sensitivity is towards λ.

When M is at the medium level ($M = 1.5$), the sensitivity of Sh_x is similar to that when M is in the low level except for the fact that the constant positive sensitivity of Sh_x towards

Table 7 Sensitivity of Nu_x and Sh_x.

B	C	Sensitivity					
		$\frac{\partial Nu_x}{\partial A}$	$\frac{\partial Sh_x}{\partial A}$	$\frac{\partial Nu_x}{\partial B}$	$\frac{\partial Sh_x}{\partial B}$	$\frac{\partial Nu_x}{\partial C}$	$\frac{\partial Sh_x}{\partial C}$
	−1	0.049500	−0.005112	−0.1742	0.000402	−0.1755	0.000752
−1	0	0.049500	−0.005112	−0.0774	0.000182	−0.1755	0.000752
	1	0.049500	−0.005112	0.0194	−0.000038	−0.1755	0.000752
	−1	0.049500	−0.005112	−0.1742	0.000402	−0.0787	0.000532
0	0	0.049500	−0.005112	−0.0774	0.000182	−0.0787	0.000532
	1	0.049500	−0.005112	0.0194	−0.000038	−0.0787	0.000532
	−1	0.049500	−0.005112	−0.1742	0.000402	0.0181	0.000312
1	0	0.049500	−0.005112	−0.0774	0.000182	0.0181	0.000312
	1	0.049500	−0.005112	0.0194	−0.000038	0.0181	0.000312

(a)

(b)

(c)

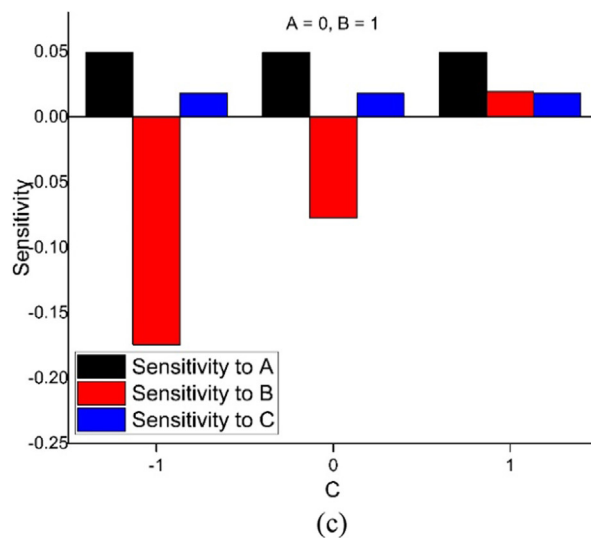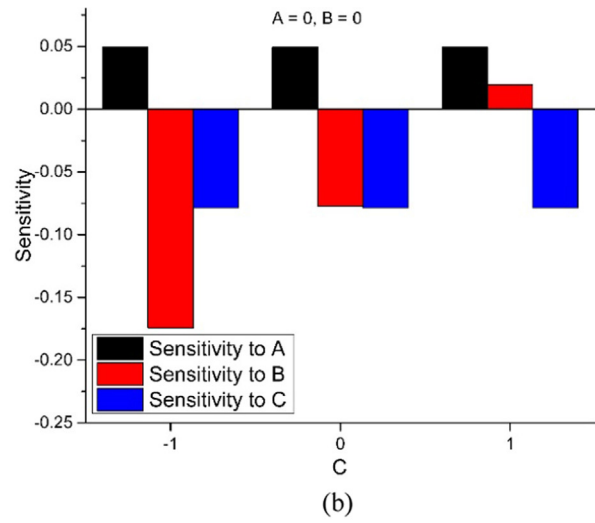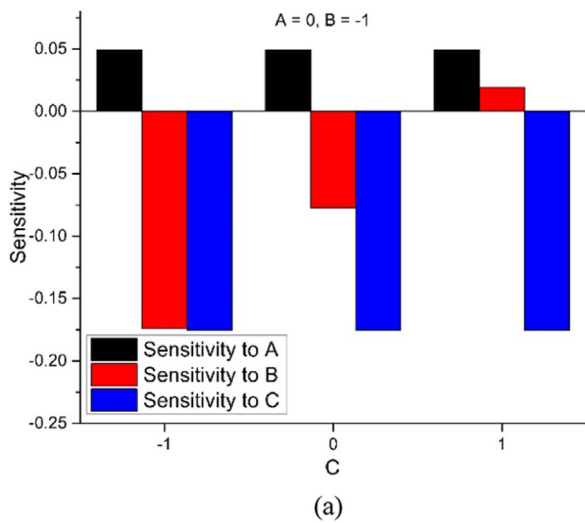**Fig. 31** Sensitivity Analysis of Nu_x.
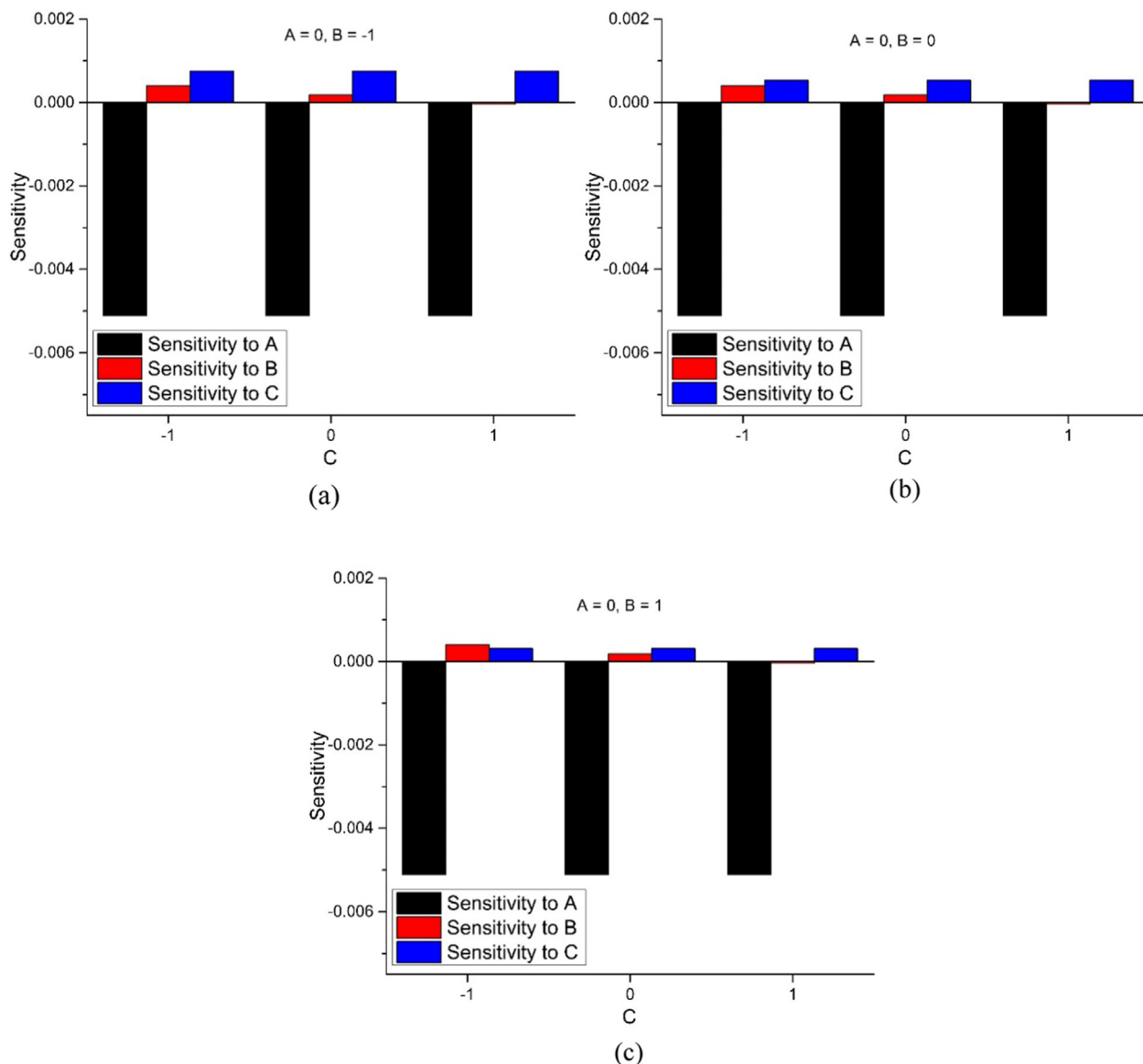
Fig. 32   Sensitivity Analysis of Sh_x.

Table 8   Comparison of the work.

C_{fx} (Present)	Nu_x (Present)	C_{fx} [53]	Nu_x [53]	Sh_x (Present)	Sh_x [53]
-1.44440	-1.44441	-0.157972	-0.157985	-0.0700232	-0.0700246
-1.55681	-1.55687	-0.159352	-0.159359	-0.0729415	-0.0729417
-1.68828	-1.68827	-0.159941	-0.159950	-0.0752265	-0.0752292
-1.6460	-1.65463	-0.159201	-0.159203	-0.0770811	-0.0770810

λ has decreased (see Fig. 32(b)). The constant positive sensitivity of Sh_x towards λ has further decreased when M is at the high level (see Fig. 32(c)). Therefore, when $\lambda = 0.1$, the highest positive sensitivity of Sh_x is M.

7.9. Comparison of the work with published literature

It is necessary to check the accuracy of the solution. For that purpose, the HAM solution is used to evaluate $C_f Re_x^{1/2}$, Nu_x

and Sh_x to show the correlation. Table 8 shows that the HAM solution has a fantastic agreement with the solution of Runge-Kutta Fehlberg method along with Shooting method [53].

8. Conclusions

The piece of note investigates probable error and statistical declaration, sensitivity analysis in Casson nanofluid with heat

and mass transfer, magnetohydrodynamics, buoyancy effects, heat source/sink, thermal radiation, binary chemical reaction and activation energy. Thermal disorderedness is also discussed. The ANOVA table given in Table 5 measures the accuracy of the estimated model.

The following conclusions can be drawn from the present exploration:

- Velocity decays for larger Stefan blowing parameter.
- Heat source enhances the fluid temperature, and heat sink reduces the temperature of the fluid.
- Concentration decreases as the Schmidt number is increased.
- Surface drag force reduces for higher Casson fluid parameter while the reverse behaviour is observed for surface heat and mass transfer rates.
- Strengthening of Brinkman number, Casson fluid parameter, diffusive variable, temperature ratio variable, concentration ratio variable and activation energy leads to a rise in entropy generation rate.
- The reduced Nusselt number is directly proportional to the Stefan blowing parameter and inversely proportional to the magnetic parameter and the stretching/shrinking parameter.
- The reduced Sherwood number is inversely proportional to the Stefan blowing parameter and the magnetic parameter and stretching/shrinking parameter have only a nominal effect.
- The sensitivity of the reduced Nusselt number towards stretching/shrinking parameter is the highest when the magnetic parameter is at the low level ($M = 0.5$)
- The positive sensitivity of the reduced Sherwood number towards the magnetic parameter decreases for low and medium levels of stretching/shrinking parameter and is negligible for the high level of stretching/shrinking parameter.
- The reduced Nusselt and Sherwood number have respectively a constant positive and negative sensitivity for Stefan blowing parameter for all levels of magnetic parameter and stretching/shrinking parameter.
- Prandtl number quantity is used which refers to the human blood.
- Comparison of the present work shows an excellent agreement with the previous work.

Declaration of Competing Interest

The authors declare that they have no known competing financial interests or personal relationships that could have appeared to influence the work reported in this paper.

Acknowledgements

References

[1] T. Hayat, M.I. Khan, M. Waqas, A. Alsaedi, M. Farooq, Numerical simulation for melting heat transfer and radiation effects in stagnation point flow of carbon-water nanofluid, Comput. Methods Appl. Mech. Engrg. (2016) 1–32.

[2] T. Hayat, M.I. Khan, M. Farooq, T. Yasmeen, A. Alsaedi, Stagnation point flow with Cattaneo-Christov heat flux and homogeneous-heterogeneous reactions, J. Mol. Liquids 220 (2016) 49–55.

[3] M.I. Khan, M. Waqas, T. Hayat, A. Alsaedi, Colloidal study of Casson fluid with homogeneous-heterogeneous reactions, J. Colloid Interf. Sci. (2017).

[4] T. Hayat, M.I. Khan, T.A. Khan, M.I. Khan, S. Ahmad, A. Alsaedi, Entropy generation in Darcy-Forchheimer bidirectional flow of water-based carbon nanotubes with convective boundary conditions, J. Mol. Liquids (2018).

[5] M.W.A. Khan, M.I. Khan, T. Hayat, A. Alsaedi, Entropy generation minimization (EGM) of nanofluid flow by a thin moving needle with nonlinear thermal radiation, Phys. B: Condens. Matter 534 (2018) 113–119.

[6] T. Hayat, M.I. Khan, A. Alsaedi, M.I. Khan, Joule heating and viscous dissipation in flow of nanomaterial by a rotating disk, Int. Commun. Heat Mass Transf. 89 (2017) 190–219.

[7] M. Rashid, M.I. Khan, T. Hayat, M.I. Khan, A. Alsaedi, Entropy generation in flow of ferromagnetic liquid with nonlinear radiation and slip condition, J. Mol. Liquids (2018).

[8] T. Hayat, M.I. Khan, M. Farooq, A. Alsaedi, M. Waqas, T. Yasmeen, Impact of Cattaneo-Christov heat flux model in flow of variable thermal conductivity fluid over a variable thicked surface, Int. J. Heat Mass Transf 99 (2016) 702–710.

[9] S. Qayyum, M.I. Khan, T. Hayat, A. Alsaedi, M. Tamoor, Entropy generation in dissipative flow of Williamson fluid between two rotating disks, Int. J. Heat Mass Transf 127 (2018) 933–942.

[10] T. Hayat, S. Qayyum, M.I. Khan, A. Alsaedi, Current progresses about probable error and statistical declaration for radiative two phase flow using Ag-H2O and Cu-H2O nanomaterials, Int. J. Hydrogen Energy (2017).

[11] S. Qayyum, T. Hayat, M.I. Khan, M.I. Khan, A. Alsaedi, Optimization of entropy generation and dissipative nonlinear radiative Von Karman's swirling flow with Soret and Dufour effects, J. Mol. Liquids (2018).

[12] T. Hayat, S.A. Khan, M.I. Khan, A. Alsaedi, Theoretical investigation of Ree-Eyring nanofluid flow with entropy optimization and Arrhenius activation energy between two rotating disks, Comput. Meth. Programs Biomed. 177 (2019) 57–68.

[13] M.I. Khan, S. Qayyum, T. Hayat, M.I. Khan, A. Alsaedi, T.A. Khan, Entropy generation in radiative motion of tangent hyperbolic nanofluid in presence of activation energy and nonlinear mixed convection, Phys. Lett. A (2018).

[14] T. Hayat, M.I. Khan, S. Qayyum, A. Alsaedi, Entropy generation in flow with silver and copper nanoparticles, Colloids Surfaces A 539 (2018) 335–346.

[15] N. Casson, A flow equation for pigment-oil suspensions of the printing ink type. Rheology of disperse systems, 1959.

[16] G. Alotta, E. Bologna, G. Failla, M. Zingales, A Fractional Approach to Non-Newtonian Blood Rheology in Capillary Vessels, J. Peridyn. Nonl. Model. (2019) 1–9.

[17] M.M. Rashidi, Z. Yang, M.M. Bhatti, M.A. Abbas, Heat and mass transfer analysis on MHD blood flow of Casson fluid model due to peristaltic wave, Therm Sci 22 (2018) 2439–2448.

[18] W.P. Walawender, T.Y. Chen, D.F. Cala, An approximate Casson fluid model for tube flow of blood, Biorheology 12 (2) (1975) 111–119.

[19] S. Shehzad, T. Hayat, A. Alsaedi, MHD flow of a Casson fluid with power law heat flux and heat source, Comput. Appl. Math. 37 (3) (2018) 2932–2942.

[20] R. Mehmood, S. Rana, N. Akbar, S. Nadeem, Non-aligned stagnation point flow of radiating Casson fluid over a stretching surface, Alexandr. Eng. J. 57 (2) (2018) 939–94621.

[21] M. Archana, B. Mahanthesh, Exploration of activation energy and binary chemical reaction effects on nano Casson fluid flow with thermal and exponential space-based heat source, Multidiscip. Model. Mater. Struct. 15 (1) (2019) 227–245.

[22] O. Makinde, N. Sandeep, T. Ajayi, I. Animasaun, Numerical exploration of heat transfer and Lorentz force effects on the flow of MHD Casson fluid over an upper horizontal surface of a thermally stratified melting surface of a paraboloid of revolution, Int. J. Nonl. Sci. Num. Simul. 19 (2) (2018) 93–106.

[23] Z. Shah, S. Islam, H. Ayaz, S. Khan, Radiative heat and mass transfer analysis of micropolar nanofluid flow of Casson fluid between two rotating parallel plates with effects of Hall current, J. Heat Transfer 141 (2) (2019) 022401.

[24] G. Seth, M. Mishra, Analysis of transient flow of MHD nanofluid past a non-linear stretching sheet considering Navier's slip boundary condition, Adv. Powder Technol. 28 (2) (2017) 375–384.

[25] P. Besthapu, R.U. Haq, S. Bandari, Q.M. Al-Mdallal, Thermal radiation and slip effects on MHD stagnation point flow of non-Newtonian nanofluid over a convective stretching surface, Neural Comput. Appl. 31 (1) (2019) 207–217.

[26] S.Z. Alamri, R. Ellahi, N. Shehzad, A. Zeeshan, Convective radiative plane Poiseuille flow of nanofluid through porous medium with slip: an application of Stefan blowing, J. Mol. Liq. 273 (2019) 292–304.

[27] T. Hayat, S. Nadeem, A. Khan, Rotating flow of Ag-CuO/H 2 O hybrid nanofluid with radiation and partial slip boundary effects, Eur. Phys. J. E 41 (6) (2018) 75.

[28] B. Mahanthesh, B. Gireesha, R.S. Gorla, O.D. Makinde, Magnetohydrodynamic three-dimensional flow of nanofluids with slip and thermal radiation over a nonlinear stretching sheet: a numerical study, Neural Comput. Appl. 30 (5) (2018) 1557–1567.

[29] M. Rashid, M.I. Khan, T. Hayat, M.I. Khan, A. Alsaedi, Entropy generation in flow of ferromagnetic liquid with nonlinear radiation and slip condition, J. Mol. Liq. 276 (2019) 441–452.

[30] M. Irfan, W. Khan, M. Khan, M.M. Gulzar, Influence of Arrhenius activation energy in chemically reactive radiative flow of 3D Carreau nanofluid with nonlinear mixed convection, J. Phys. Chem. Solids 125 (2019) 141–152.

[31] A. Zeeshan, N. Shehzad, R. Ellahi, Analysis of activation energy in Couette-Poiseuille flow of nanofluid in the presence of chemical reaction and convective boundary conditions, Res. Phys. 8 (2018) 502–512.

[32] M.I. Khan, A. Alsaedi, S. Qayyum, T. Hayat, M.I. Khan, Entropy generation optimization in flow of Prandtl-Eyring nanofluid with binary chemical reaction and Arrhenius activation energy, Colloids Surf. A: Physicochem. Eng. Asp. 570 (2019) 117–126.

[33] T. Hayat, A. Aziz, T. Muhammad, A. Alsaedi, Numerical simulation for Darcy-Forchheimer 3D rotating flow subject to binary chemical reaction and Arrhenius activation energy, J Central South Univ. 26 (5) (2019) 1250–1259.

[34] M. Irfan, M. Khan, Simultaneous impact of nonlinear radiative heat flux and Arrhenius activation energy in flow of chemically reacting Carreau nanofluid, Appl. Nanosci. (2019) 1–12.

[35] S. Rashid, M.I. Khan, T. Hayat, M. Ayub, A. Alsaedi, Theoretical description of Arrhenius energy in binary chemically rotating mixed convective flow with radiative flux, Appl. Nanosci. (2019) 1–9.

[36] S. Shehzad, T. Hussain, T. Hayat, M. Ramzan, A. Alsaedi, Boundary layer flow of third grade nanofluid with Newtonian heating and viscous dissipation, J. Central South Univ. 22 (1) (2015) 360–367.

[37] S. Qayyum, T. Hayat, S.A. Shehzad, A. Alsaedi, Nonlinear convective flow of Powell-Erying magneto nanofluid with Newtonian heating, Res. Phys. 7 (2017) 2933–2940.

[38] I. Khan, M. Saqib, A.M. Alqahtani, Channel flow of fractionalized H2O-based CNTs nanofluids with Newtonian heating, Discr. Contin. Dyn. Syst.-S (2019) 176–183.

[39] T. Hayat, I. Ullah, B. Ahmad, A. Alsaedi, Radiative flow of Carreau liquid in presence of Newtonian heating and chemical reaction, Res. Phys. 7 (2017) 715–722.

[40] A. Hussanan, M.Z. Salleh, I. Khan, R.M. Tahar, Heat and mass transfer in a micropolar fluid with Newtonian heating: an exact analysis, Neural Comput. Appl. 29 (6) (2018) 59–67.

[41] M. Imtiaz, T. Hayat, M. Hussain, S. Shehzad, G. Chen, B. Ahmad, Mixed convection flow of nanofluid with Newtonian heating, Eur. Phy. J. Plus 129 (5) (2014) 97.

[42] S.A. Shehzad, Magnetohydrodynamic Jeffrey nanoliquid flow with thermally radiative Newtonian heat and mass species, Revista Mexicana de Física 64 (6) (2018) 628–633.

[43] M.I. Khan, A. Kumar, T. Hayat, M. Waqas, R. Singh, Entropy generation in flow of Carreau nanofluid, J Mol. Liq. 278 (2019) 677–687.

[44] M.I. Khan, S. Qayyum, T. Hayat, M. Waqas, M.I. Khan, A. Alsaedi, Entropy generation minimization and binary chemical reaction with Arrhenius activation energy in MHD radiative flow of nanomaterial, J. Mol. Liq. 259 (2018) 274–283, https://doi.org/10.1016/j.molliq.2018.03.049.

[45] R. Ellahi, A. Zeeshan, F. Hussain, A. Asadollahi, Peristaltic Blood Flow of Couple Stress Fluid Suspended with Nanoparticles under the Influence of Chemical Reaction and Activation Energy, Symmetry 11 (2) (2019) 276, https://doi.org/10.3390/sym11020276.

[46] K.G. Kumar, M.R. Krishnamurthy, N.G. Rudraswamy, Boundary layer flow and melting heat transfer of Prandtl fluid over a stretching surface by considering Joule heating effect, Multidiscip. Model. Mater. Struct. 15 (2) (2019) 337–352, https://doi.org/10.1108/mmms-03-2018-0055.

[47] M. Nawaz, R. Naz, M. Awais, Magnetohydrodynamic axisymmetric flow of Casson fluid with variable thermal conductivity and free stream, Alexandr. Eng. J. 57 (3) (2018) 2043–2050, https://doi.org/10.1016/j.aej.2017.05.016.

[48] H.R. Kataria, H.R. Patel, Effects of chemical reaction and heat generation/absorption on magnetohydrodynamic (MHD) Casson fluid flow over an exponentially accelerated vertical plate embedded in porous medium with ramped wall temperature and ramped surface concentration, Propul. Power Res. 8 (1) (2019) 35–46, https://doi.org/10.1016/j.jppr.2018.12.001.

[49] S.E. Ahmed, M.A. Mansour, A. Mahdy, S.S. Mohamed, Entropy generation due to double diffusive convective flow of Casson fluids over nonlinearity stretching sheets with slip conditions, Eng. Sci. Technol. Int. J. 20 (6) (2017) 1553–1562, https://doi.org/10.1016/j.jestch.2017.10.002.

[50] J. Mackolil, B. Mahanthesh, Exact and statistical computations of radiated flow of nano and Casson fluids under heat and mass flux conditions, J. Comput. Des. Eng. (2019).

[51] G.E. Box, K.B. Wilson, On the experimental attainment of optimum conditions, J. Roy. Stat. Soc.: Series B (Methodological) 13 (1) (1951) 1–38.

[52] S.Q. Chan, F. Aman, Mansur S (2018) Sensitivity Analysis on Thermal Conductivity Characteristics of a Water-Based Bionanofluid Flow Past a Wedge Surface, Math. Probl. Eng. (2018).

[53] S.M. Vahedi, A.H. Pordanjani, A. Raisi, A.J. Chamkha, Sensitivity analysis and optimization of MHD forced convection of a Cu-water nanofluid flow past a wedge, Eur. Phys. J. Plus 134 (3) (2019) 124.

[54] N.S. Khan, P. Kumam, P. Phatiphat, Second law analysis with effects of Arrhenius activation energy and binary chemical reaction on nanofluid flow, Sci. Rep. 10 (2020) 1226.